University of Nevada, Reno

Numerical Simulation of Potential Groundwater Contaminant Pathways from Hydraulically Fractured Oil Shale in the Nevada Basin and Range Province

A thesis submitted in partial fulfillment of the
requirements for the degree of Master of Science in
Hydrogeology

by

Susan C. Rybarski

Dr. Greg M. Pohll/Thesis Advisor

December, 2015

THE GRADUATE SCHOOL

We recommend that the thesis
prepared under our supervision by

SUSAN C. RYBARSKI

Entitled

Numerical Simulation Of Potential Groundwater Contaminant Pathways From Hydraulically Fractured Oil Shale In The Nevada Basin And Range Province

be accepted in partial fulfillment of the
requirements for the degree of

MASTER OF SCIENCE

Greg M. Pohll, Ph.D., Advisor

Ronald L. Hershey, Ph.D., Committee Member

Clay A. Cooper, Ph.D., Committee Member

Glenn C. Miller, Ph.D., Graduate School Representative

David W. Zeh, Ph. D., Dean, Graduate School

December, 2015

ABSTRACT

In recent years, hydraulic fracturing (fracking) has become an increasingly popular method for extraction of oil and natural gas from tight formations. Concerns have been raised over a number of environmental risks associated with fracking, including contamination of groundwater by fracking fluids, upwelling of deep subsurface brines, and methane migration. Given the potentially long time scale for contaminant transport associated with hydraulic fracturing, numerical modeling remains the best practice for the assessment of migration of fracking fluids. Oil shale in the upper Humboldt Basin of northeastern Nevada has now become a target for hydraulic fracturing operations. Analysis of regional groundwater flow is used to assess several potential migration pathways specific to the geology and hydrogeology of this basin. The model domain in all simulations is defined by the geologic structure of the basin as determined by deep oil and gas well bores and formation outcrops. Vertical transport of gaseous methane along a density gradient is simulated in TOUGH2, while fluid transport along faults and/or hydraulic fractures and lateral flow through more permeable units adjacent to the targeted shale are modeled in FEFLOW.

Sensitivity analysis considers basin, fault, and hydraulic fracturing parameters, and results highlight key processes that control fracking fluid and methane migration. Results indicate that migration of detectable concentrations is unlikely, and only one of the three migration scenarios tested showed potential for any transport to a shallow water aquifer. Any migration would be of concentrations several orders of magnitude below detection limits, and would be dependent on a number of very specific conditions. For

migration of fracking fluids, these conditions include 1) hydraulic fractures connecting the Elko shale with the adjacent carbonate formation, 2) the presence of a continuous, conductive fault connecting the adjacent carbonate formation with an overlying shallow water aquifer, 3) significant mountain block recharge in the Ruby Mountains, 4) carbonate hydraulic conductivity at a minimum of 0.1-1 m/d, 5) metamorphic core complex hydraulic conductivity on the order of 0.005 m/d or higher, and 6) fracking fluid constituents with very low to moderate sorption parameters.

CONTENTS

LIST OF TABLES

LIST OF FIGURES

INTRODUCTION

Background

In recent years, hydraulic fracturing (fracking) has become an increasingly popular method for extraction of oil and natural gas from low permeability formations. Concerns have been raised over a number of environmental risks associated with fracking, most notably including contamination of groundwater by fracking fluids, upwelling of deep subsurface brines, and methane migration (Vengosh, 2013). While these risks are theoretically preventable, studies on the effects of ongoing fracking operations on local water quality have been limited, and the environmental viability of this practice remains controversial.

Given the potentially long time scale for contaminant transport associated with hydraulic fracturing, numerical modeling remains the best practice for migration assessment. Recent studies modeling potential contaminant pathways (Myers, 2012; Gassiat et al., 2013) have attempted to analyze transport mechanisms within simplified, hypothetical or generalized basins. These studies conclude that contamination of shallow groundwater may be possible, but the results have been criticized as being inapplicable to proposed fracking sites as the boundary conditions used to drive groundwater flow in the models would almost certainly be inappropriate for real world conditions (Saiers and Barth, 2012; Carter et al., 2013).

Oil shale in the upper Humboldt Basin of northeastern Nevada has now become a target for hydraulic fracturing operations. The basin and range geology of this region has produced an environment atypical for unconventional oil extraction, and the

environmental consequences may therefore be unpredictable. Given the limited freshwater resources of the region, any operation that may potentially cause groundwater contamination warrants an in depth study.

Objectives

The objectives of this study are a) to make a geological and hydrogeological assessment of the upper Humboldt Basin as necessary to create a domain for numerical modeling, b) to determine the potential contaminant migration pathways specific to this basin, c) to create a series of cross-sectional models depicting transport along these migration pathways, and d) to analyze the sensitivity of the models to various input parameters.

Study Area

The currently proposed locations for hydraulic fracturing lie in three exploration areas in the eastern Humboldt Basin adjacent to the Ruby Mountains and East Humboldt Range (Figure 1). At the time of this writing, two wells in Exploration Area 2 and one well in Exploration Area 1 have been drilled and fracked. As the first area to be explored, and therefore the area with the greatest amount of data available, the geology and hydrogeology of Exploration Area 2 will serve as the basis for the modeling study. The study area will nevertheless consist of the entire Humboldt basin as oil and gas well logs basin-wide will be used to assess regional flow paths and formation properties.

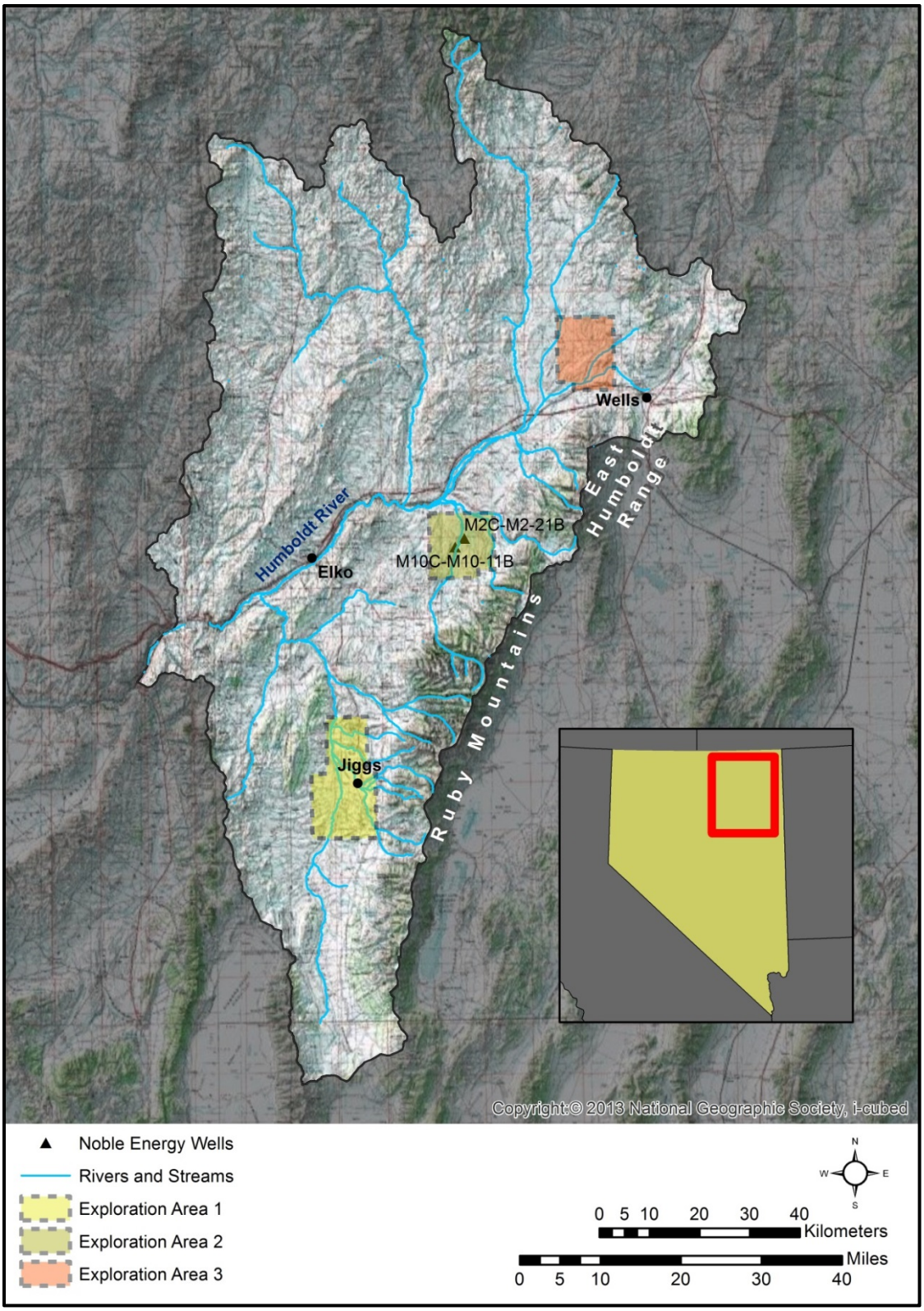

Figure 1. Study area - Upper Humboldt Basin and Noble Energy exploration areas

Geology

The exploration areas overlie a narrow structural basin paralleling the Ruby Mountains and the East Humboldt Range, which holds a thick sequence of interbedded volcanic rocks and Quaternary and Tertiary age basin-fill deposits, and which is bound to the east by a listric range front fault. A generalized stratigraphic column for the eastern Great Basin of Nevada and Utah, taken from Anna et al., (2007), provides a broad overview of the subsurface geology found in this area (Figure 2). For the eastern Nevada section, the Oligocene Indian Well and Elko Formations and the Mississippian Diamond Peak and Chainman Formations are identified as being either source rocks, oil reservoirs, or both. This section also notably depicts a ubiquitous carbonate unit of Permian and Pennsylvanian age dividing these oil-bearing Oligocene and Mississippian rocks.

At the time of this writing, two wells have been drilled in Exploration Area 2 (M2C-M2-21B and M10C-M10-11B, Figure 1). Noble Energy has provided well logs for both drill sites, which show the same general geologic structure with variations in formation depths and thicknesses. Well logs show basin-fill deposits composed of tuff, welded tuff, siltstone, claystone, and sandstone to average depth of 6730 feet, likely containing the Humboldt Formation. Underlying this sequence is the Indian Well Formation, composed largely of welded tuff and tuffaceous sandstone, with an average thickness of 1330 feet, followed by the targeted Elko Formation. The Elko Formation is a sedimentary Oligocene deposit composed of interbedded claystone, siltstone, shale, limestone, and tuff.

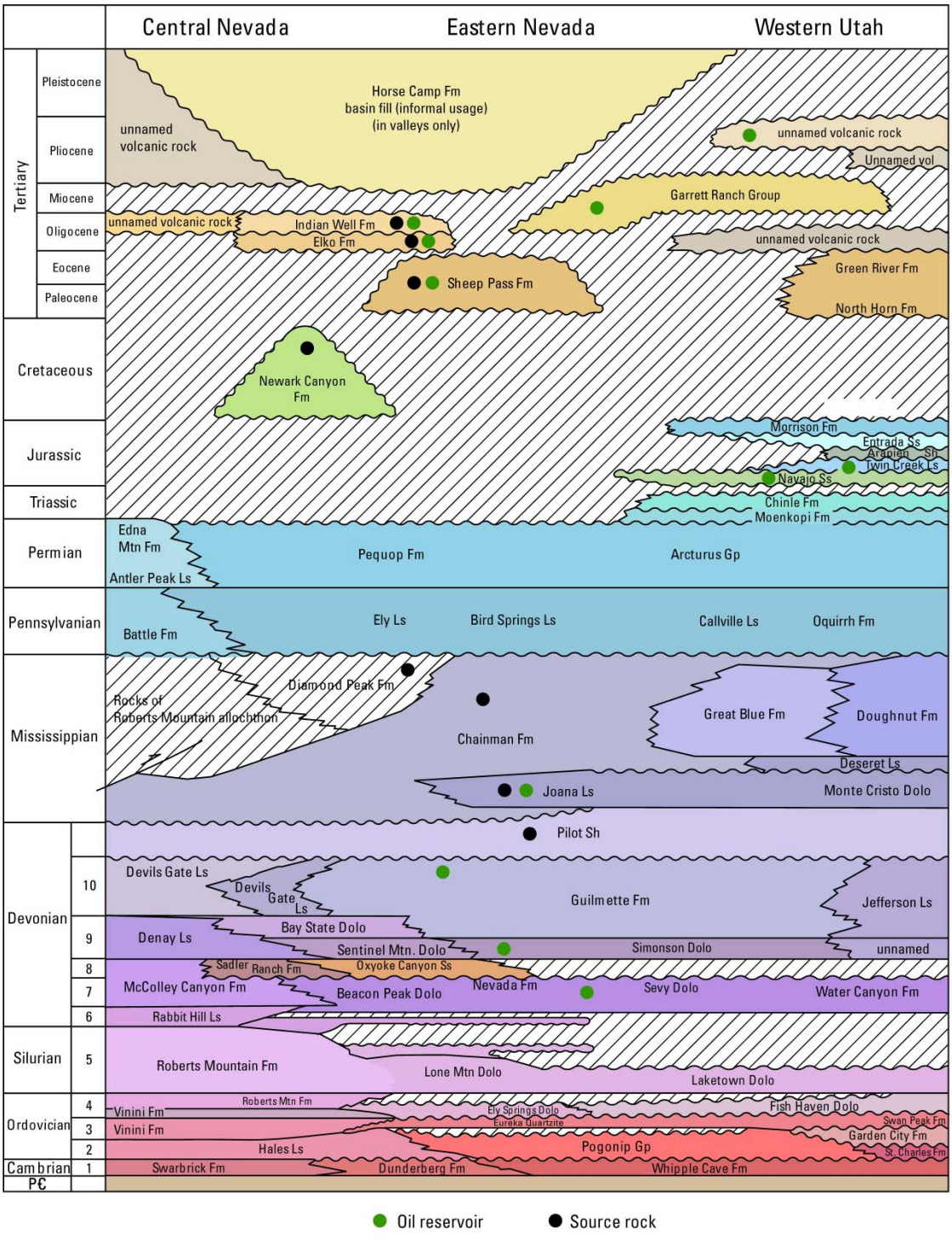

Figure 2. Generalized stratigraphic column of the eastern Great Basin of Nevada and Utah, *from* Anna et al 2007.

Well log data for M2C-M2-21B places the Elko Formation at 7610-8307 feet depth, for a total thickness of 697 feet. At this well location, the Elko Formation is primarily composed of welded tuff and tuffaceous sandstone until a depth of ~7880 feet, where the lithology is largely shale. Mud logs indicate that within the Elko Formation, oil is confined to the shale unit, giving a total reservoir thickness of ~427 feet. This well was hydraulically fractured in March 2014, with 250,057 gallons of fluid used in the process (NDOM, 2014).

Well log data for M10C-M10-11B places the Elko Formation at 8510-9060 feet depth, for a total thickness of 550 feet. At this well location, the Elko Formation is composed of interbedded shale and volcanic rocks from 8510-8940 feet depth, with thick sequences of tuffaceous sandstone and welded tuff at intervals of up to 110 feet. The thickest shale interval reaches ~50 feet. From 8940-9060 feet depth, the formation is composed entirely of siliciclastic breccia and dolomite, for a total potential reservoir thickness of 430 feet. This well was hydraulically fractured in June 2014, with 345,660 gallons of fluid used (NDOM, 2014).

Hydrogeology

Shallow groundwater in the exploration areas receives recharge from the mountain ranges to the east and flows to the west at maximum water table depths of 300-400 feet below land surface, discharging on valley floors and generally flowing north-northwest to the Humboldt River from Exploration Areas 1 and 2, and south-southwest from Exploration Area 3 (Plume, 2009). The Upper Humboldt Basin has been subdivided into

nine hydrographic areas (Figure 3). Several estimates for the volume of mountain block recharge into each of these areas are summarized in Table 1.

Table 1. Estimates of mountain block recharge for upper Humboldt Basin hydrographic areas.

Source	42	43	44	45	46	47	48	49	50	Total
	(afy)	(afy)	(afy)	(afy)	(afy)	(afy)	(afy)	(afy)	(afy)	(afy)
Nowlin, 1986						15,000				
Rush and Everett, 1966					3,000	14,000	13,000			
Eakin and Lamke, 1966	83,000							13,000		
State of Nevada, 1971	54,000	26,000	58,000	36,000	4,000	14,000	13,000	7,400	8,000	220,400
Masbruch, 2011 (In-place + runoff)	51,000	42,000	46,000	17,000	13,000	48,000	28,000	3,600	6,100	254,700
Masbruch, 2011 (In-place only)	31,000	18,000	30,000	5,900	8,700	45,000	5,800	2,900	5,200	152,500
Maxey-Eakin, 1949 - Calculated	48,000	31,000	56,000	29,000	20,000	49,000	13,000	7,000	7,000	260,000
Epstein, 2004 Calculated	73,000	98,000	71,000	65,000	52,000	83,000	18,000	10,000	7,000	477,000
Average	51,400	43,000	52,200	30,580	19,540	47,800	15,560	6,180	6,660	272,920

Regional groundwater flow in the basin is poorly understood, but may also occur through deeper carbonate layers underlying these basin-fill deposits, and the flow direction is expected to be similar to the shallow groundwater flow (Prudic, 1995).

To more easily characterize the hydrogeology of the region, the formations composing the basin stratigraphy relevant to this study can be generalized into several hydrogeologic units, following Plume (2009). In order of increasing age:

Younger basin-fill deposits consist of unconsolidated Quaternary alluvium.

Older basin-fill deposits are composed of Tertiary sedimentary deposits including claystone, siltstone, sandstone, shale and limestone, and are often interbedded with volcanic rocks. Included here are the Elko, Indian Well, Humboldt, and Hay Ranch

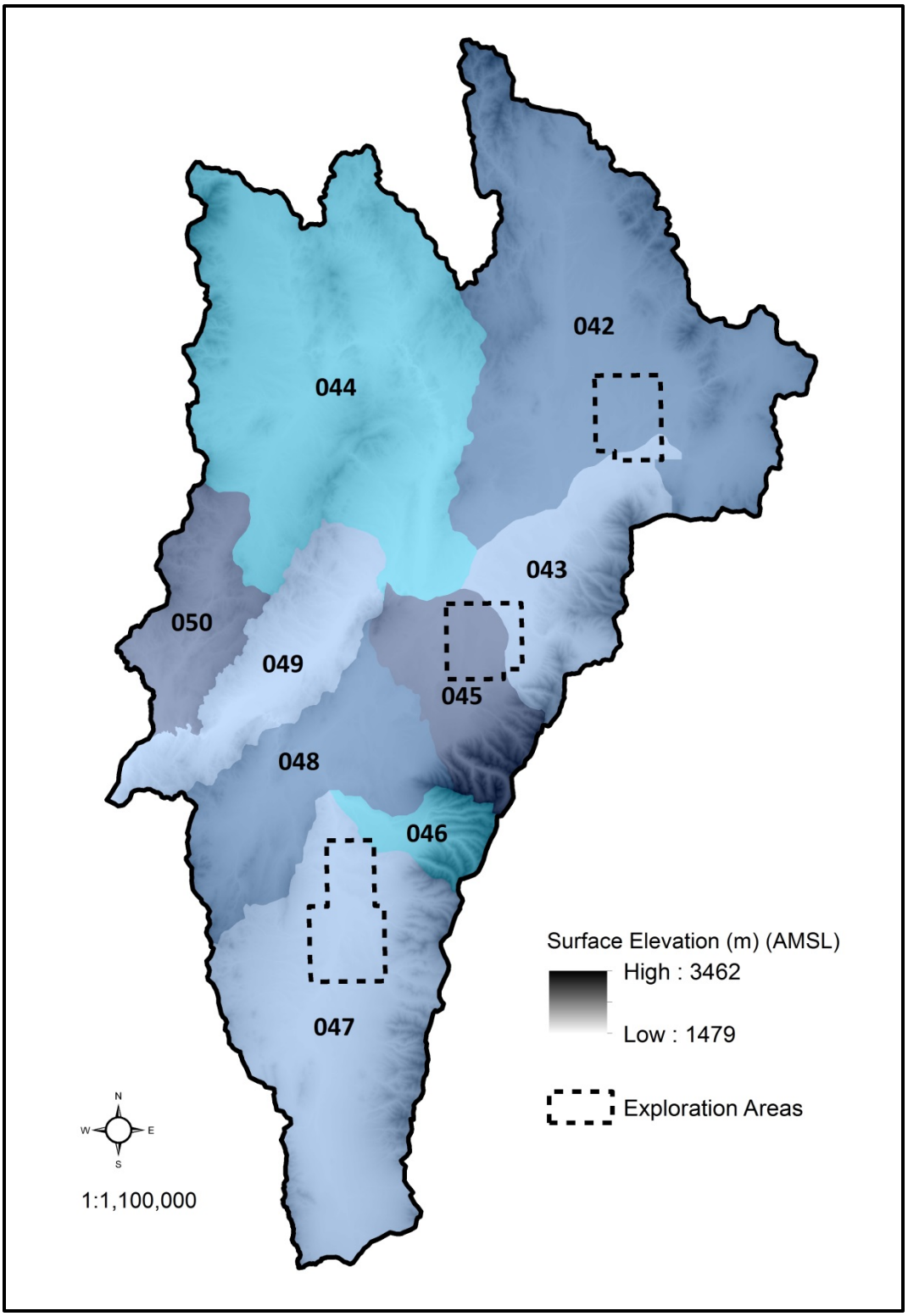

Figure 3. Upper Humboldt Basin hydrographic areas.

Formations. Estimates of the hydraulic conductivity (K) of these deposits range from 2 to 40 ft/d, based on sediments at gold mines along the Carlin Trend west of the basin and driller's logs from selected wells near the Humboldt River, which may be applicable to sediments in the Upper Humboldt basin (Plume, 1996). For the purposes of this study, only sediments of Miocene age or younger will be generalized as such, and separate values for hydraulic properties of the Elko and Indian Well Formations will be estimated.

Volcanic rocks of Eocene to Holocene age appear as deposits interbedded with younger and older basin fill deposits, and are largely composed of welded tuffs and rhyolite.

Upper Paleozoic carbonates form thick sequences of limestones of Permian and Pennsylvanian age. Drill logs from the two exploration wells indicate that these carbonates appear directly below the target Elko Formation in Exploration Area 2. Carbonate rock aquifer tests conducted in both upper and lower Paleozoic carbonates throughout the Great Basin have found hydraulic conductivities ranging from 0.0005 to 900 ft/d (Plume, 1996), with the wide variability presumably due to localized faulting, fracturing, and/or dissolution. However, none of these tests were conducted in the Humboldt basin.

Lower Paleozoic carbonates form thick sequences of dolomites and limestones of Devonian or lower Mississippian to Ordovician age, and include the Joana and Devil's Gate Limestones, the Guilmette Formation, and the Bay State, Sentinel Mountain and Simonson Dolomites.

Mississippian clastic rocks are composed largely of shales and sandstones and include the Diamond Peak and Chainman Formations, as well as the Pilot Shale. These shales have been the target for many of the previously drilled oil and gas wells, but drill logs from the exploration wells in Area 2 do not indicate the presence of oil or gas in these formations in this area.

Literature Review

Hydraulic Fracturing

Hydraulic fracturing is used to increase the permeability of tight reservoirs which would otherwise not produce economically viable quantities of oil and gas. Fluid pressure in the target formation is increased by pumping in a mixture of water and fracking fluids until the pressure exceeds the tensile strength of the formation rocks, causing them to fracture. Proppant is then injected to hold the fractures open and allow for extraction of resources. Fractures open in the direction of least principal stress and propagate in the direction of greatest principal stress. At the depth of most fracking operations, the greatest principal stress is almost always due to the overburden, and fractures therefore propagate vertically. Given the extensional tectonic conditions at the proposed fracking sites and depth of the target formation, vertical fracture propagation can be safely assumed.

A recent study (Davies et al., 2012) examined the reported heights of stimulated hydraulic fractures over several thousand fracturing operations in shale reservoirs. This review found that the maximum reported vertical fracture extent reached ~588 meters (1929 ft). However, this was an extreme outlier as the probability of a stimulated fracture

exceeding 350 vertical meters (1148 ft) was reported as less than 1%, with the majority of fractures extending to less than 100 vertical meters (328 ft). It should be noted that this data set does not include unintentionally stimulated hydraulic fractures, which may occur during well blowouts or during waste water injection following resource extraction. One such event occurred at the Tordis Field offshore Norway, where injected waste water from oil production resulted in a 900 meter (2953 ft) fracture. However, this was the result of a continuous 5.5 month injection period, while typical fracking injection events are less than 2 hours.

For hydraulic fracturing events occurring at depths for which the least principal stress is horizontal and the greatest principal stress is vertical, it may be possible to estimate the vertical extent of fractures. Assuming no leakoff, the volume of a fracture will be equal to the volume of fluid injected, and the ratio of fracture extent to aperture will be determined by mechanical properties of the rock and formation pressure. A study detailed in Flewelling 2013, analyzed fracture heights estimated from microseismic data and compared these heights to injected fluid volumes to derive an equation for maximum fracture extent:

$$H = \left[\frac{3\Omega V E}{\pi a P_n (1-\nu^2)}\right]^{\frac{1}{3}} \quad (1)$$

where H is the fracture height, V is the volume of injected fluid, $\Omega \approx \sqrt{1 + 1.464a^{1.65}}$ is a shape parameter, a is the fracture aspect ratio, P_n is the net pressure (fluid pressure less the least compressive stress), E is Young's modulus, and ν is Poisson's ratio. Flewelling

demonstrates the efficacy of this equation as a predictor of maximum potential fracture height given the volume of injected fluid in Figure 4.

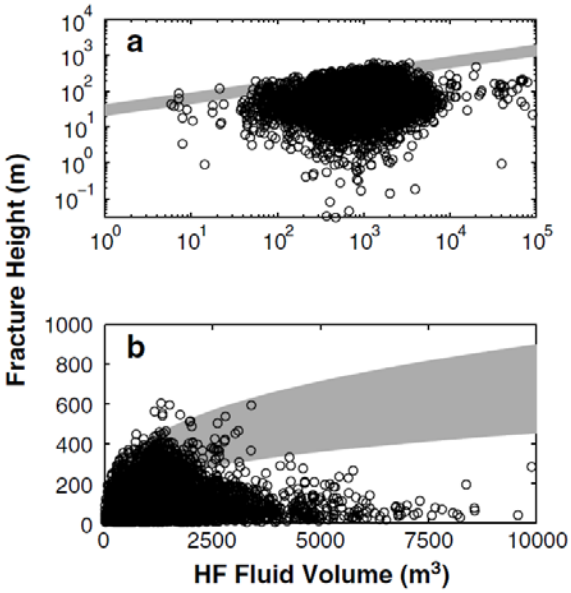

Figure 4. Fracture heights relative to injected fluid volumes, *from* Flewelling 2013.

Modeling Studies

As concerns about the potential consequences of hydraulic fracturing have been raised, several studies have attempted to model the process to determine the likelihood of failure. The methods and results used in three models of note will be summarized here. The first, detailed in Myers 2012, was run in MODFLOW-2000 as a 1-D vertical flow system with a model domain consisting of a simple, evenly spaced 450 meter (1476 ft) square with bottom layers representing a tight shale unit and overlying layers representing a sandstone overburden unit, in effort to create a simplified representation of the Marcellus shale. Myers attempts to model five scenarios for transport, beginning with estimated K values for the shale and sandstone units and transport driven by constant head boundaries. He creates additional scenarios with the addition of a high K 'fault', and then alters the K value of the shale to simulate fracturing in models with and without the fault to determine the time to equilibrium. Finally, he simulates the changes in flux and potentiometric surface given the injection of

fluid in a horizontal well. Ultimately, the study concluded that contamination of a shallow aquifer could occur in as little as 10 years following hydraulic fracturing.

Myers' model has been criticized (Saiers and Barth, 2012 and Carter et al., 2013) for his failure to address the effects of multiphase transport, fluid densities, and temperature variations. Additionally, the model parameters were criticized as being so simplistic, and/or based on isolated and unrepresentative data points, as to be unrepresentative of the Marcellus shale, and it was stated that the calculated transport times could therefore not be assumed valid. A number of mathematical errors and conflicting results have also been noted (Cohen et al., 2013), with the suggestion that the model likely did not converge and incomplete QA/QC was undertaken.

The second modeling effort of note, detailed in Kissinger et al 2013, was run in DuMu^x with a 3-D model domain as a 1000x1000 meter (3281 ft) square column with a depth of 2000 meters (6562 ft) and cell size varying from 10 to 100 meters (32.8 to 328 ft). This study attempted to simulate the potential for transport of brine, fracking fluid, and methane gas for prospective hydraulic fracturing sites in Germany, and investigated three scenarios: 1) fracking fluid flow along fractures connected to a pre-existing natural fault zone, where the short-term pressure gradient due to fracturing is the driving force, 2) long-term transport (30 years) of fracking fluids along an up-dip geological profile, where natural horizontal and vertical pressure gradients are the driving force, and 3) long-term (100 years) transport of methane gas through the overburden along a density gradient, where a permeable fault zone penetrating the overburden is present. Scenarios 1 and 2 were analyzed as single phase (water) systems, where fracking fluids were treated

as a conservative tracer. Scenario 3 was analyzed as a two-phase (brine and methane gas) system, where methane was assumed to behave as an ideal gas.

This study differed from the Myers simulations in its consideration of densities and viscosities of brine and methane, allowance for multiphase flow (for scenario 3 only) and lateral transport, and use of a temperature gradient. Because this study attempted to model a natural gas reservoir, an oil phase was not considered. The simulations for the first scenario showed limited vertical transport (maximum of 50 meters or 164 feet) given a fracture induced pressure gradient persisting for 2 hours, and allowing for fractures extending through the reservoir to the overburden.

Second scenario simulations do not include the pressure gradient induced by fracturing, and instead assume that a given amount of fracking fluids have penetrated the overburden. Models showed that given a permeable fault zone and artesian conditions, the density gradient of the brine at depth could be overcome and contamination of the shallow layers would be possible – though only under very conservative conditions, and with a notable decrease in contaminant concentration from that at depth.

The third scenario does not explicitly model fractures connecting the reservoir and overburden, but instead assumes a constant flux of methane. The simulations allow for methane to be transported as a dissolved gas in brine or in gas phase depending on the pressure and temperature, which are assumed to follow hydrostatic and geothermal gradients. These simulations indicated that leakage of methane into shallow layers through the overburden would be possible, but would only occur given a shallow reservoir containing large volumes of methane, a permeable fault zone penetrating the full thickness of the overburden, and low residual saturation and low porosity. Models

also showed large amounts of methane transported over the lateral boundaries due to capillary forces.

The final modeling effort of note is detailed in Gassiat et al., 2013, which describes a two-dimensional, single-phase, multispecies and density dependent finite element numerical model run in SUTRA-MS, partially in effort to resolve some of the criticisms of the model described in Myers, 2012. Also unlike the site specific model described in Kissinger et al., 2013, this study attempts to create a generic basin by compiling publicly available data of shale gas basins and fracking operations, rather than modeling a specific hydraulic fracturing site.

Within the framework of the hypothetical basin, a sensitivity analysis was conducted to determine the sensitivity of contaminant transport to the range of parameters found in the shale gas basin data set. The parameters analyzed include permeabilities and porosities of the shale and overlying units, topographic gradient, matrix compressibility, pressure gradient in the shale, salinity and depth to saline formations, depth to and thickness of the shale gas formation, distance between pre-existing faults, length of fracking zone and vertical extent of fractures, and the permeability of the fracking zone following fracturing operations.

For all simulations, a worst case scenario fault extending from the shale fracture zone to a shallow aquifer is assumed, and contaminants are assumed to be conservative. Additionally, the study assumes that the initial pressure pulse resulting from hydraulic fracturing will have a negligible effect on transport, and begins simulations following fracking operations. Hydraulic fractures are also assumed confined within the shale unit. Given these conditions, the simulations indicated that when hydraulic fracturing occurs in

the middle of a shale formation, the most important parameters controlling contaminant transport are those that control migration to the fault: pressure gradient in the shale, thickness of the shale above the fracture zone, and fault permeability in the shale.

METHODS

Potential Migration Pathways

As part of an ongoing study, the United States Environmental Protection Agency (EPA) has identified six potential mechanisms for fluid migration resulting from hydraulic fracturing of a shale reservoir (EPA, 2012), summarized here:

1. Defective or insufficient well construction coupled with excessive pressure during hydraulic fracturing, resulting in well casing failure and fluid migration through casing cement.
2. Fracturing of the overburden resulting in a hydraulic connection between the targeted shale and a more permeable adjacent unit, allowing fluid migration.
3. Fracturing of the overburden resulting in fluid communication between the targeted shale and a more permeable adjacent unit, after intercepting an additional overlying hydrocarbon reservoir which acts as an additional source of contaminants.
4. Activation of sealed/dormant fractures or faults, creating pathways for upward migration of fluids.

5. Fracturing of the overburden creates pathways for fluid migration to nearby wells with deteriorating well casings, which may in turn intercept more permeable units.
6. Fracturing of the overburden creates pathways for fluid migration to nearby wells which have been improperly closed, and which may have compromised well casings, allowing a low resistance pathway to a more permeable unit or groundwater aquifer.

Not specifically identified by the EPA as mechanisms for fluid migration are the following:

7. Methane degassing as reservoir pressure decreases following hydraulic fracturing and during subsequent pumping, and the potential for vertical transport along a density gradient.
8. The potential for horizontal contaminant flow along an adjacent permeable unit.

This study disregards well construction and surface spill issues, and instead focuses on the potential for fluid migration resulting from fractures allowing fluid communication between shale and adjacent units, or the reactivation of faults. While fracture communication with an overlying unit is possible, at depths of over 7500 feet below the surface, and with no evidence of a strong vertical pressure gradient, flow of fracking fluids to the surface in the absence of pre-existing fracture networks or faults is extremely unlikely (Davies et al., 2012; Flewelling, 2013). Additionally, oil and gas well logs from wells in or near the targeted exploration areas do not indicate a hydrocarbon reservoir

overlying the Elko Formation. This study will therefore investigate the likelihood of scenarios 4, 7 and 8 only, detailed here as:

Fractured Carbonate Scenario – The targeted Elko shale is underlain by a fractured carbonate unit which may act as a conduit for regional flow, receiving recharge in the Ruby Mountains or East Humboldt Range in the east and flowing to the west. In this scenario, hydraulic fractures penetrate the contact between the shale and carbonate units, and fracking fluid is transported through the carbonate unit along the existing flow path (Figure 5).

Fault Connectivity Scenario – In this scenario, hydraulic fractures penetrate upward into the overlying Indian Well Formation, connecting with a hypothetical pre-existing or reactivated fault zone. Although a connection between the fracture and fault is made, the induced pressure is only enough to transport fluid to the end of the fracture. Migration through the fault may then occur given the natural flow regime and an initial concentration at the base of the fault (Figure 6).

Methane Degassing Scenario – Less specific to hydraulic fracturing, though still a potential migration pathway for hydraulic fracturing operations, is vertical migration of gaseous methane. Pumping creates a zone of low fluid pressure surrounding the borehole. This decrease in pressure allows dissolved methane in the formation water to come out of solution as a gas. While pumping continues, this gas will be drawn towards the borehole – however, the return to equilibrium fluid pressure in the formation is not immediate

following the cessation of pumping. The remaining gaseous methane may then travel vertically along a density gradient (Figure 7).

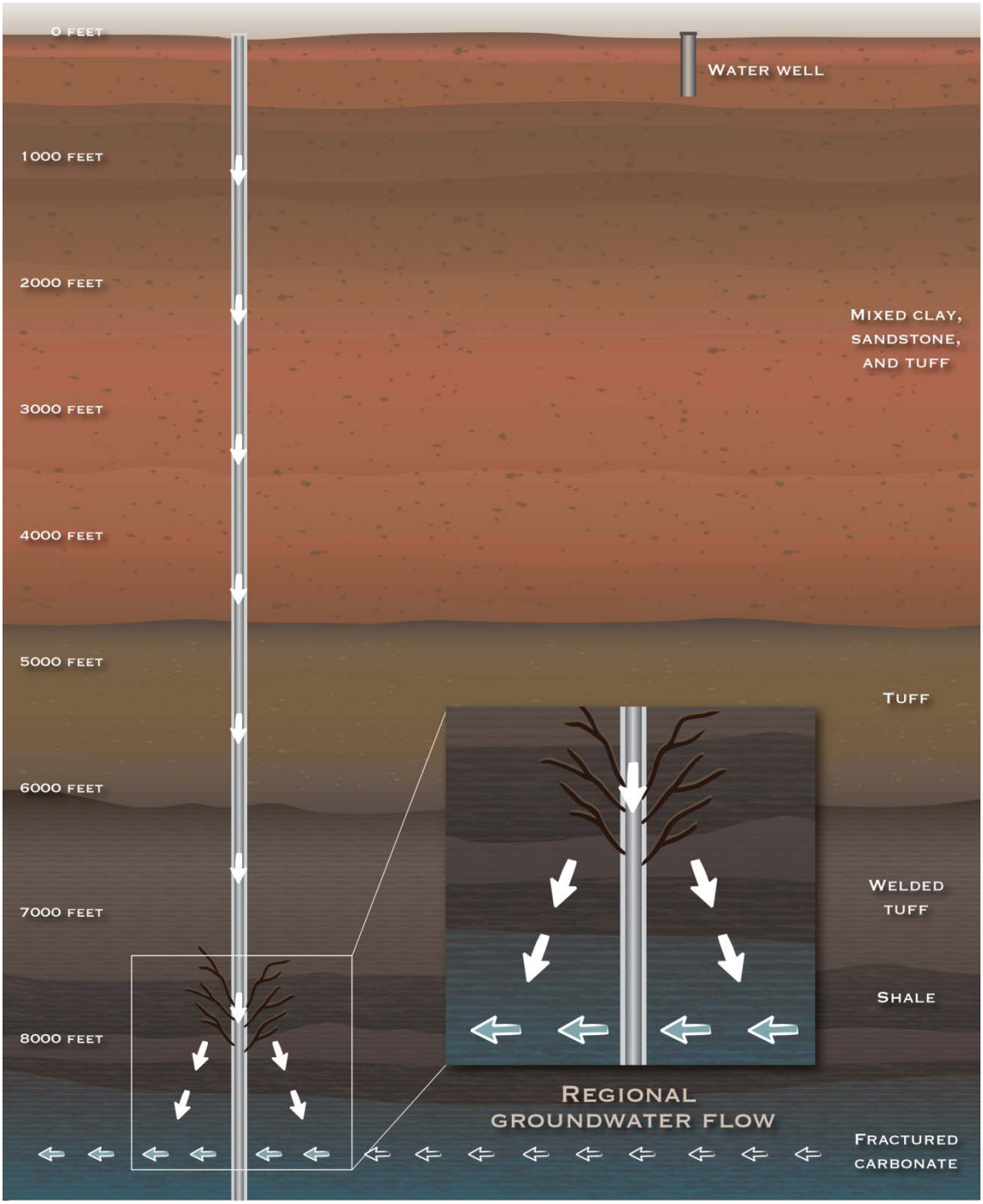

Figure 5. Fractured Carbonate Scenario - Fracking fluid enters the carbonate formation underlying the targeted Elko shale, and is transported along a regional flow path.

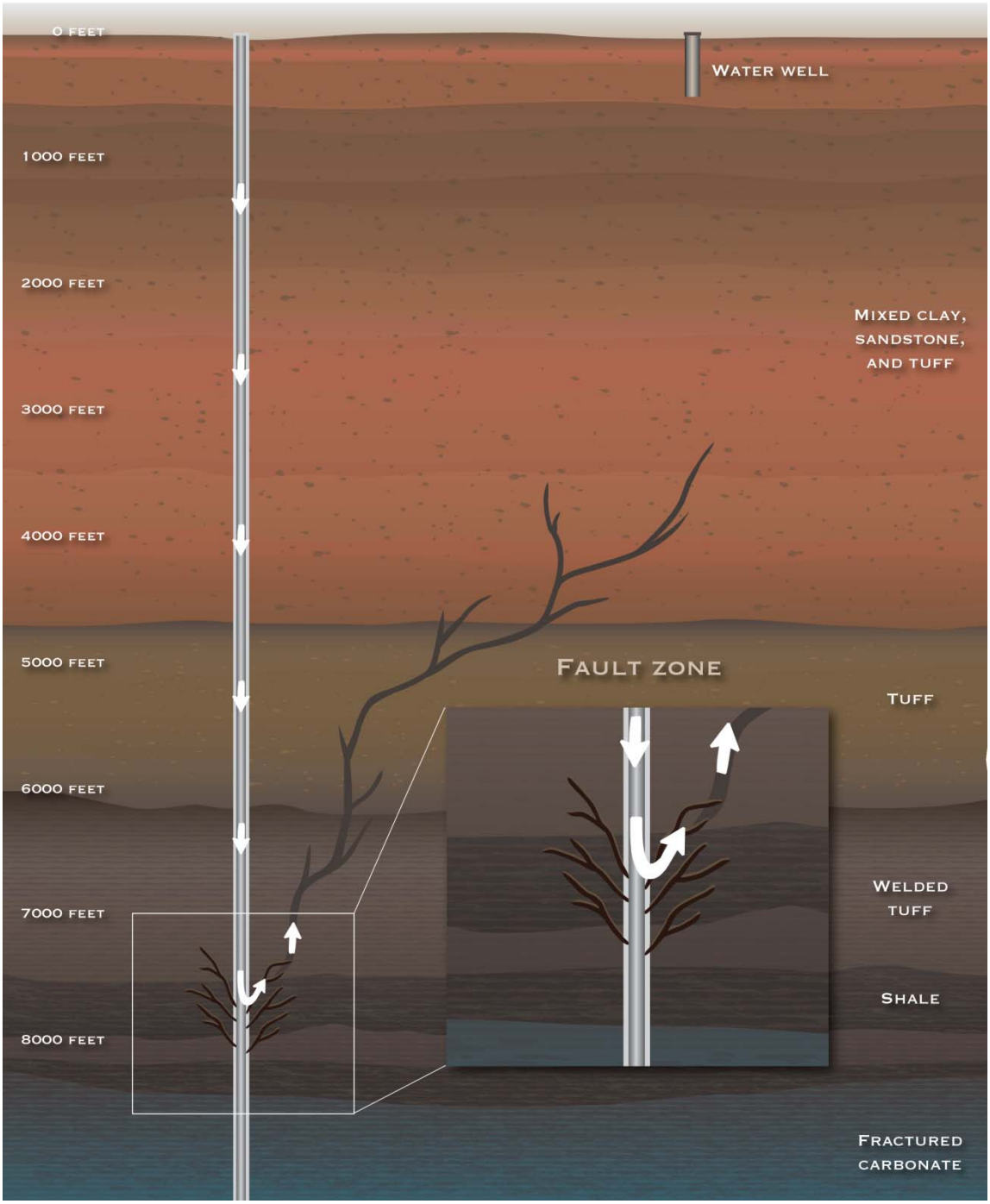

Figure 6. Fault Connectivity Scenario - Hydraulic fractures connect with a pre-existing or reactivated fault, fracking fluids are transported along a natural flow regime.

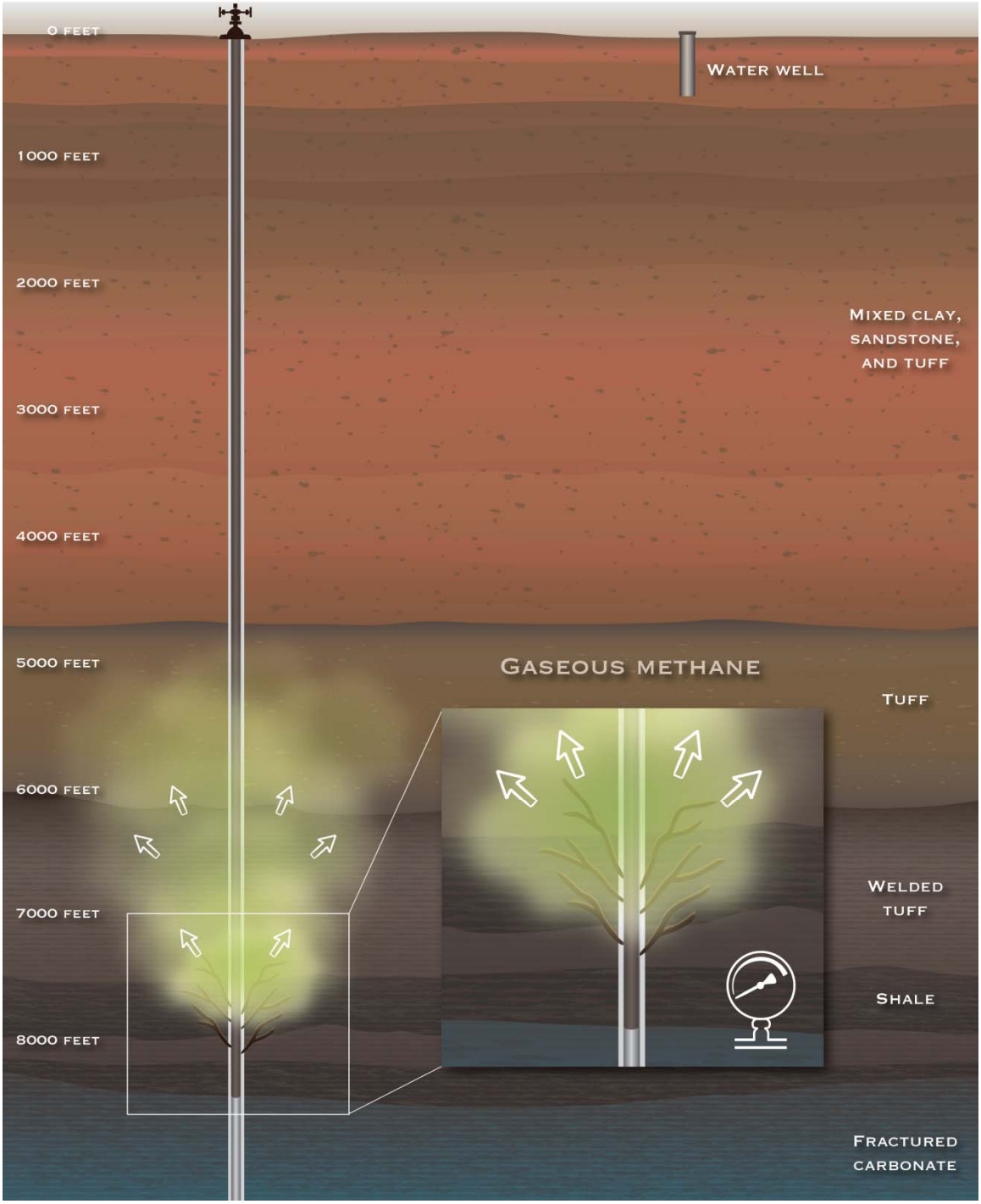

Figure 7. Gaseous Methane Scenario - Formation pressure drops due to pumping, dissolved methane degasses and is transported vertically along a density gradient.

Study Site

To examine the potential for lateral migration of fracking fluids through the underlying fractured carbonate formation, or vertical migration through a pre-existing fault, an east/west cross-section representative of the geology of Exploration Area 2 was developed for use as a two-dimensional model domain. Well logs for all oil and gas wells in the upper Humboldt Basin (Hess et al., 2011), including those provided by Noble Energy, were analyzed for any available lithological data, and depths to formation tops were compiled (Appendix A). Together with Mesozoic and Paleozoic outcrop elevations (Figure 8), these point depths were interpolated in ArcGIS to derive the general structure of the contact between the Elko Formation and the underlying Paleozoic carbonate rocks, referred to from this point as the Cenozoic basement. Uncertainties arise where data is sparse, and therefore two geologic interpretations for this cross-section are presented and modeled in this report, such that the more likely interpretation (Figure 11a) is used as the base scenario for sensitivity analysis and the less likely interpretation (Figure 11b) is modeled only once to highlight the difference in transport resulting from this alternate interpretation.

In the Elko Hills to the west of Exploration Area 2, geologic maps (Coats, 1987 and Ketner, 1990) show outcrops of the Indian Well, Elko, and Diamond Peak Formations, as well as carbonate formations of Permian and Pennsylvanian age (Figure 10). These maps also indicate a series of east dipping normal faults along the eastern front of the Elko Hills. These faults are contrasted by the west dipping range front fault structures along the western front of the Ruby Mountains to the east of Exploration Area 2, exhibiting a

structure typical of basin and range geology. Minor outcrops of Permian or Pennsylvanian age carbonates can also be found in the Ruby Mountains directly to the east of Exploration Area 2.

A transect A-A' was selected beginning in the carbonate outcrop in the Ruby Mountains, running west to intersect Noble Energy's M2C-M2-21B exploration well, then proceeding on a northwest tangent towards the Humboldt River, creating an approximation of the expected shallow aquifer and regional flow paths (Figures 9, 10). Using the Cenozoic basement interpolation as the basis for the overall basin structure along A-A', the Chainman, Diamond Peak, Carbonate, Elko, and Indian Well Formations were then stacked along this transect, assuming a constant thickness for each as determined by the thicknesses observed in the M2C-M2-21B well log. These formations were overlain to known surface elevation by Tertiary basin fill deposits and Quaternary alluvium as indicated by geologic maps (Coats, 1987), and this generalized cross-section was then adjusted to incorporate a basin and range fault structure. Because it is unclear whether the carbonate formation extends from depth to the outcrop at the eastern side of the basin, or whether this outcrop is simply an isolated remnant (more likely), two cross-sections are presented (Figure 11a, 11b).

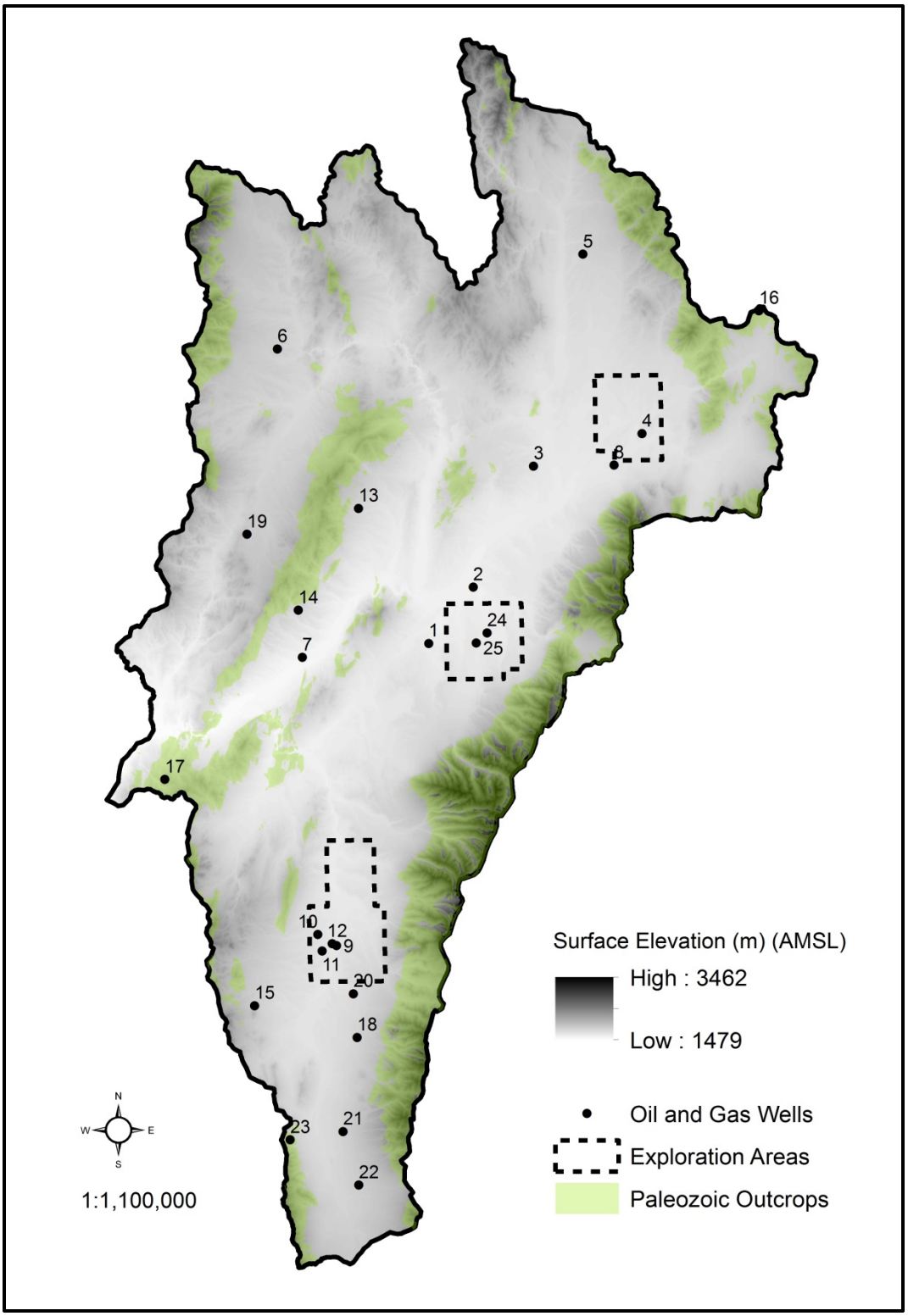

Figure 8. Locations of upper Humboldt Basin oil and gas wells and Paleozoic outcrops used in depth interpolation.

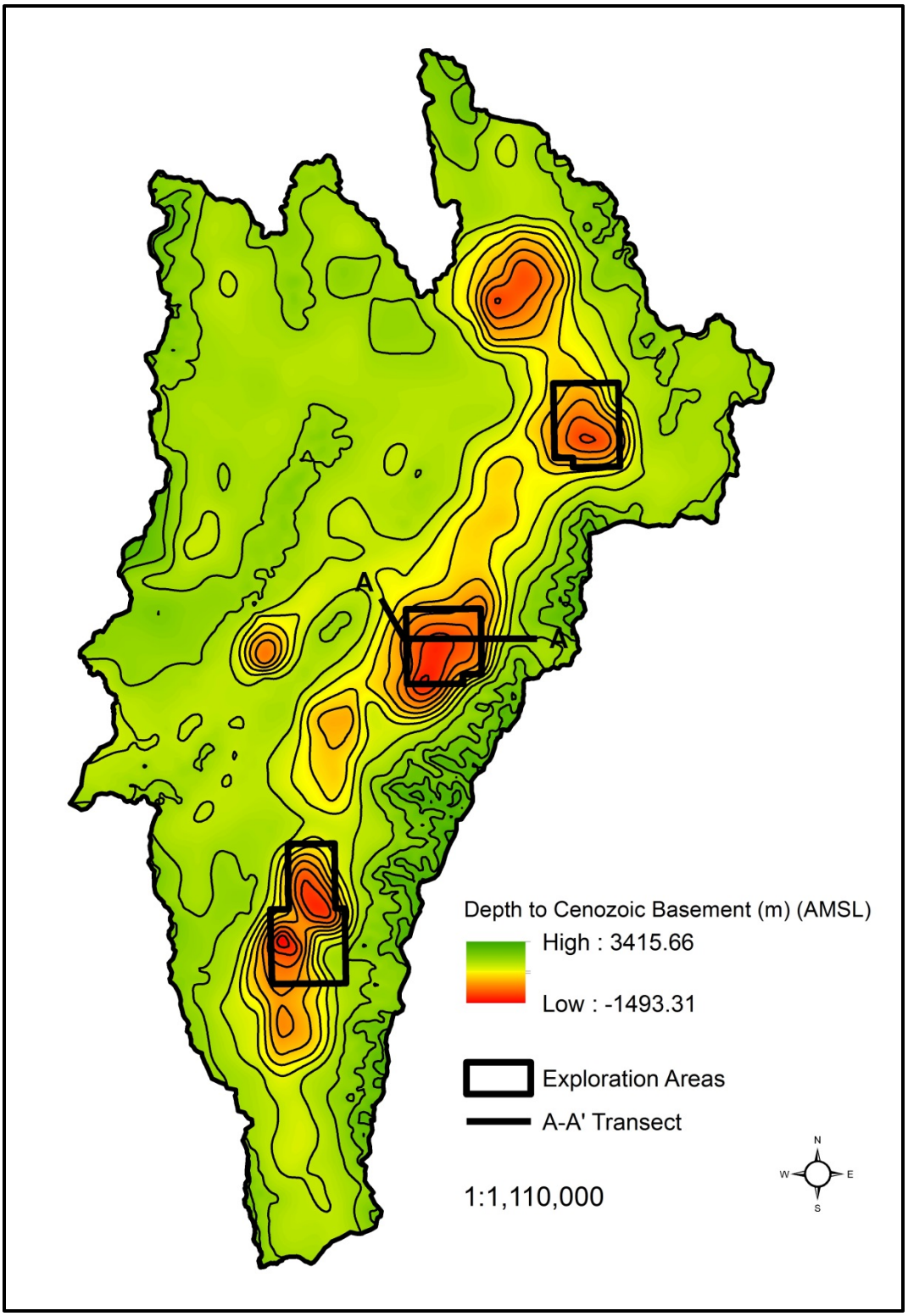

Figure 9. Structure of contact between Elko Formation and underlying Paleozoic carbonates.

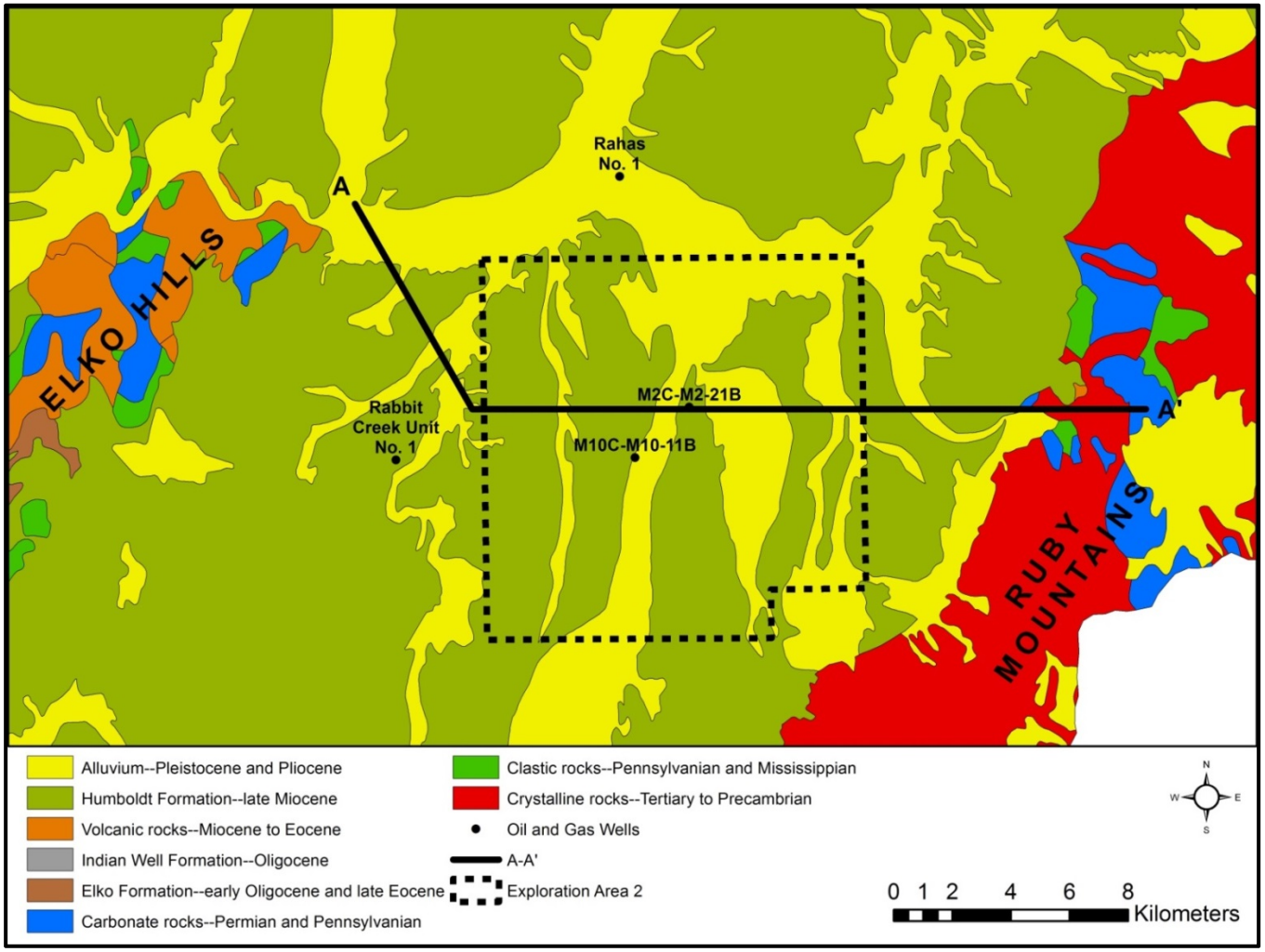

Figure 10. Location of cross-section A-A' through Exploration Area 2 and local surface geology

a.

b.

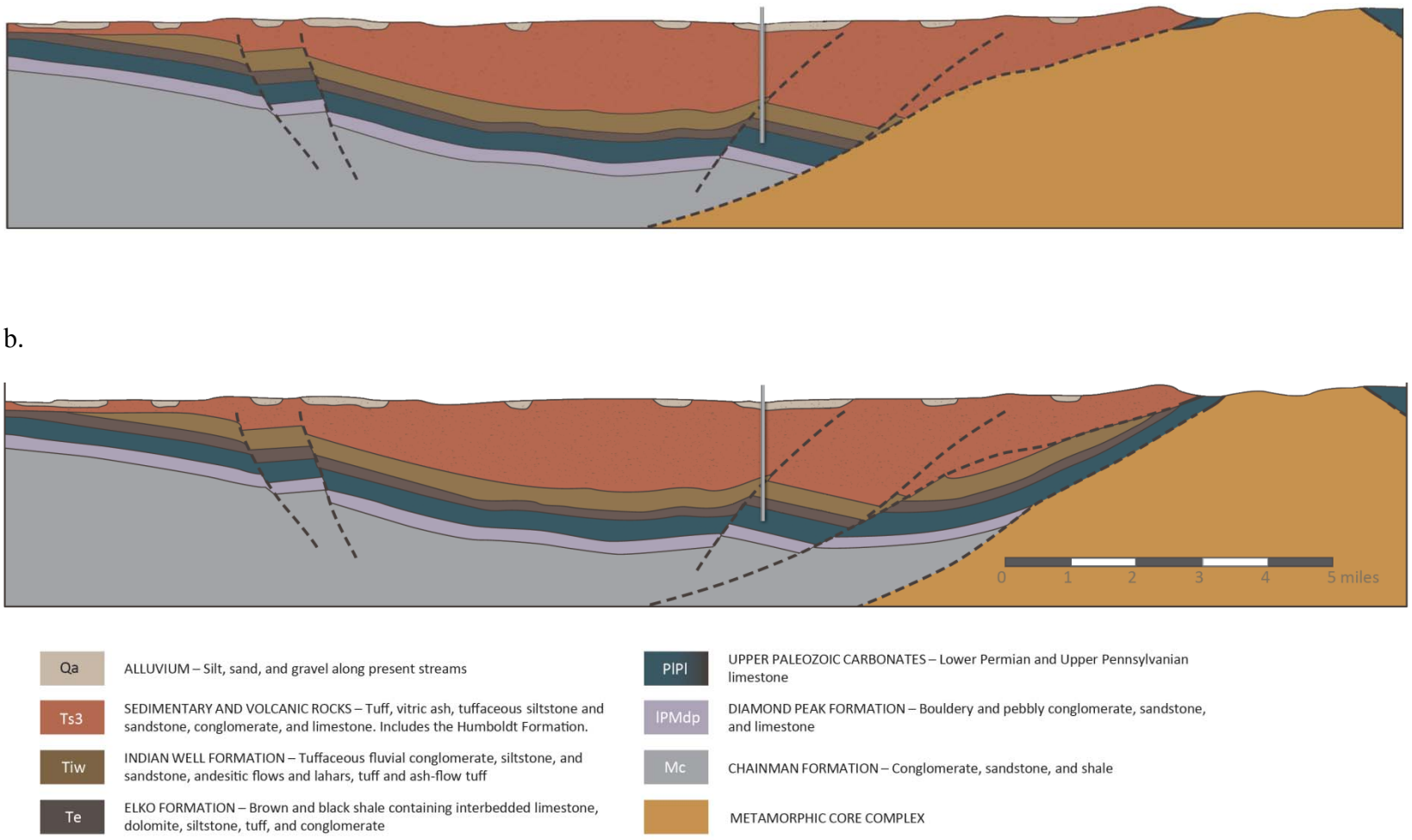

Figure 11. a) Interpolated geology at cross-section A-A', base scenario, b) Alternative geological interpretation

Conceptual Models

Fractured Carbonate Scenario

This scenario explores the potential for contaminant transport along a regional flow path through a fractured carbonate formation underlying the targeted oil shale, in the case of hydraulic fracture connectivity between the shale and carbonate formations. The model places a mass concentration representative of fracking fluids in the carbonate formation near its upper boundary, and simulates single-phase flow of a dissolved tracer.

Both the fractured carbonate scenario detailed here and the fault connectivity scenario discussed in the following section were simulated as under fully saturated conditions as 2-D vertical systems in FEFLOW. FEFLOW is a finite element modeling program for groundwater systems that simulates flow, heat, and mass transport.

The model mesh created for these scenarios follows the cross-sectional representation of the upper Humboldt basin intersecting Exploration Area 2. The transect begins in the east in the Ruby Mountains, intersects Noble Energy well M2C-M2-21B, and terminates near the Humboldt River. Formation thicknesses and porosities are taken from Noble Energy borehole logs and assumed to be constant. Hydraulic conductivities for all formations (Table 2) are taken from a combination of literature values for formations in this basin and drill stem test analyses from previously drilled wells basin-wide as discussed in a concurrent report (Pohll et al., 2015).

Table 2. Formation parameters used in FEFLOW simulations.

Formation	Hydraulic Conductivity (m/d)	Porosity	Thermal Conductivity (J/m/s/K)
Alluvium	4.0	0.50	2.9
Sedimentary and Volcanic Rocks	1.0	0.35	2.0
Indian Well Formation	0.1	0.20	1.7
Elko Formation	0.0005	0.2	2.9
Upper Paleozoic Carbonates	3.0	0.03	3.4
Diamond Peak Formation	1.0	0.05	3.4
Chainman Formation	0.0005	0.05	2.9
Metamorphic Core Complex	0.05	0.01	3.4

A fluid-flux (Neumann type) boundary condition on the eastern surface of the mesh represents recharge into the carbonate formation and basin fill deposits. Recharge values were varied for sensitivity over a range of 0.0009 - 0.006 m/d, taken from the span of possible values from several estimates of mountain block recharge into the basin (Table 1). Volumes of mountain block recharge from contributing hydrographic areas were reduced to one dimension, dividing by the length of mountain ranges in these areas and by the width of permeable carbonate and basin fill deposits only, as metamorphic rocks were assumed to be relatively impermeable. A constant hydraulic-head (Dirichlet type) boundary condition was placed on the upper bounds to the west near the Humboldt River intersection and set as the approximate elevation of the river (1600 m [5250 feet]) (Figure 12).

Formation temperatures were derived through the placement of a heat-flux (Neumann type) boundary condition along the lower boundary of the model and a constant temperature (Dirichlet type) boundary condition along the upper boundary of the model. Heat flux values for the basin range from 90-105 W/m^2 as determined from geothermal potential data for the Great Basin region (Coolbaugh et al., 2005) and were

set accordingly, with variation within that range to adjust for unrealistic resulting temperatures along the western boundary. The constant temperature boundary was set to 15°C to be representative of surface air temperatures (Figure 12). Thermal conductivities were taken from literature values for the dominant rock type in each formation (Beardsmore and Cull, 2001, pg 104).

Longitudinal dispersivity for all formations was set to 30 m (98 ft), taken from a range of possible literature values appropriate for the scale of observation (Zheng and Bennett, 2002) and selected from that range because it resulted in the most stable simulation. Transverse dispersivity was assumed to be $1/10^{th}$ of this value.

Subsurface fault data is limited away from the borehole, and hypothetical faults were placed to be consistent with a typical basin and range structure. While several faults affect basin structure, only one is modeled here as a discrete feature and potential flow path. The fault is conceptually modeled as an open rectangular slit with a constant length and width and the hydraulic aperture is varied for sensitivity over a range of 0.0001-0.01 meters.

Five sorption coefficients were simulated, to account for the range of sorption coefficients across the variety of chemicals present in fracking fluids. Organic compounds can be sorbed to organic carbon present in the aquifer, at varying rates largely dependent on the molecular structure of the compound. This process causes some solutes to migrate through the aquifer at a much slower rate than the groundwater that is transporting them (Fetter, 1999). The sorption parameters used are representative

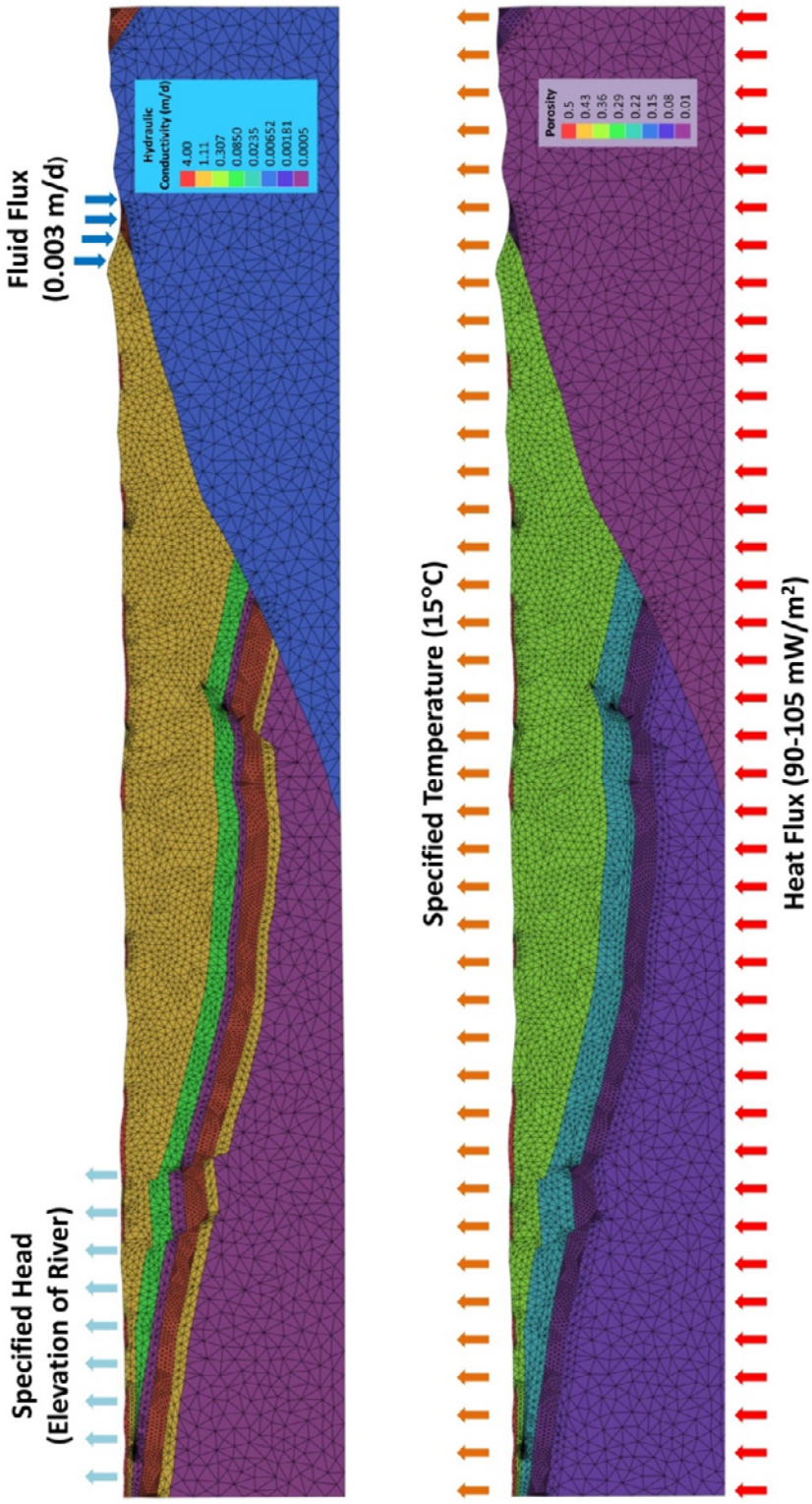

Figure 12. Boundary conditions for FEFLOW models

of ethanol (very low sorption), ethylene glycol monobutyl ether (low sorption), 2,2-dibromo-3-nitrilopropionamide (moderate sorption), hydrotreated light petroleum distillate (high sorption), and naphthalene (very high sorption). Sorption was calculated in FEFLOW using a linear adsorption isotherm, such that

$$C^* = \kappa C \tag{5}$$

where C^* is the concentration of adsorbed species in units of mass per solid volume, κ is the Henry sorptivity coefficient, and C is the concentration of the dissolved species in units of mass per fluid volume. The sorptivity coefficient κ is more often expressed in terms of the distribution coefficient K_d, where K_d is the product of the sorptivity coefficient and the bulk density of the porous media, which was assumed to be 2.65 g/cm^3 for all formations. For organic compounds, K_d can be calculated from the soil organic carbon/water coefficient (K_{oc}) of the compound and the fraction of organic carbon of a soil or aquifer surface (f_{oc}), where

$$K_d = K_{oc} f_{oc} \tag{6}$$

and for which K_{oc} and f_{oc} are determined experimentally (Fetter, 1999). Values of K_{oc} and f_{oc} were taken from literature values (Table 3).

Table 3. Distribution coefficients tested in fractured carbonate scenario

Constituent	K_{oc}	K_d Carbonate (f_{oc} = 0.0008)	K_d Humboldt (f_{oc} = 0.0006)	K_d Elko (f_{oc} = 0.0158)	K_d IW (f_{oc} = 0.0091)
Ethanol	2.7	0.00216	0.00162	0.0427	0.0246
Ethylene glycol monobutyl ether	15	0.012	0.009	0.237	0.137
2,2-Dibromo-3-nitrilopropionamide	65	0.052	0.039	1.03	0.592
Hydrotreated light petroleum distillate	800	0.64	0.48	12.64	7.28
Napthalene	18200	14.6	10.9	288	166

Because the initial concentration of solute placed in the model is also subject to the equilibrium condition with the concentration of the adsorbed species as expressed in equation 6.6, initial concentrations were scaled based on the value of κ for each constituent, such that the total initial species mass in the model domain was equal for all simulations. This initial total mass was set to 131.1 grams, that being the species mass calculated when a concentration of 1 mg/L was placed in a model domain assuming no sorption (i.e., $\kappa = 0$).

For each of the five sorption coefficients simulated, eleven potential scenarios were tested (Table 4), varying hydraulic conductivity of the carbonate, basin fill, and metamorphic rock formations, recharge volume, and fault aperture for sensitivity. For each scenario, the model was run without mass transport until steady state flow conditions were achieved. A mass concentration of 1 mg/L was then placed at a node approximately 300 feet below the contact between the Elko Formation and the carbonate formation, and the models were allowed to run for 2000 years. Nodes at depths shallower than approximately 600 feet were considered to be potentially within a shallow water aquifer and were monitored for detectable mass concentrations over the duration of the model run.

A normalized detectable concentration was calculated for each simulated constituent assuming the maximum allowable concentration was used. For example, the maximum concentration of ethanol to be included in the fracking fluid was reported to be

approximately 464 mg/L (Frac Focus, 2014). The detection limit for ethanol for the analyses used in the geochemistry portion of a concurrent study (Pohll et al., 2015) is 2

Table 4. Simulation parameters for fractured carbonate scenario

Simulation	Recharge (m/d)	Hydraulic conductivity of carbonate (m/d)	Hydraulic conductivity of Tertiary sediments (m/d)	Hydraulic conductivity of metamorphic rocks (m/d)	Hydraulic aperture of fault (m)
1	0.003	3	1	0.005	0.001
2	0.006	3	1	0.005	0.001
3	0.0009	3	1	0.005	0.001
4	0.003	40	1	0.005	0.001
5	0.003	0.01	1	0.005	0.001
6	0.003	3	2	0.005	0.001
7	0.003	3	0.01	0.005	0.001
8	0.003	3	1	0.005	0.01
9	0.003	3	1	0.005	0.0001
10	0.003	3	1	0.05	0.001
11	0.003	3	1	0.0005	0.001

mg/L, equivalent to a concentration of approximately 0.0043 mg/L in the model framework. Any simulation showing a concentration greater than 0.0043 mg/L within the upper 600 feet of the model domain (i.e., the shallow water aquifer) would therefore be indicative of a scenario allowing detectable contaminant migration. It should be noted, however, that these detection limits are representative of the capabilities of the lab used in the Pohll et al., 2015 study, and are not necessarily the lowest possible detection limits for these constituents.

Fault Connectivity Scenario

This scenario explores the potential for contaminant transport along a fault zone in the Indian Well Formation and Tertiary sediments overlying the targeted oil shale, in

the case of hydraulic fractures connecting to a pre-existing fault. The model places a mass concentration representative of fracking fluids in a fault in the Indian Well Formation near its lower boundary, and simulates single-phase transport of a conservative tracer.

The same model mesh described in the carbonate transport scenario is used here, with the same hydraulic and thermal conductivities, porosities, and boundary conditions. A fault was placed such that the base of the fault is within the Indian Well Formation, and within 400 feet of the contact between the upper boundary of the Elko shale and the well bore – the distance calculated to be the maximum potential fracture extent given the volume of water injected by the equation derived in Flewelling et al., 2013. Though the fault zone placement in this scenario differs from the carbonate transport scenario, it is conceptually modeled in the same way, and the hydraulic aperture is varied for sensitivity over the same range of values (0.0001-0.01 m).

Table 5. Simulation parameters for fault connectivity scenario

Simulation	Recharge (m/d)	Hydraulic conductivity of Indian Well (m/d)	Hydraulic conductivity of Tertiary sediments (m/d)	Hydraulic conductivity of metamorphic rocks (m/d)	Hydraulic aperture of fault (m)
1	0.003	0.1	1	0.005	0.001
2	0.006	0.1	1	0.005	0.001
3	0.003	54	1	0.005	0.001
4	0.003	0.0001	1	0.005	0.001
5	0.003	0.1	2	0.005	0.001
6	0.003	0.1	1	0.005	0.01
7	0.003	0.1	1	0.05	0.001

Seven simulations were run, in this case varying the conductivities of the Indian Well Formation and the Tertiary sediments, recharge, and fault aperture for sensitivity (Table 5). Simulations were run to steady state before the addition of a 1 mg/L concentration at the base of the fault zone, and then allowed to run for 2000 years.

Methane Degassing Scenario

This scenario explores the potential for vertical transport of near-borehole gaseous methane along a density gradient. This process was simulated as a fully saturated 2-D vertical system using TOUGH2, an integral finite difference numerical simulator for non-isothermal flows of multiphase fluids. TOUGH2 models the balance of mass and energy (i.e. heat) through the solution of equations which can be generally written as

$$\frac{d}{dt}\int_{V_n} M^{\kappa} dV_n = \int_{\Gamma_n} \mathbf{F}^{\kappa} \bullet \mathbf{n} d\Gamma_n + \int_{V_n} q^{\kappa}\, dV_n \qquad (7)$$

where V_n is an arbitrary subdomain of the flow system under study bounded by a closed surface Γ_n and n is a normal vector on that surface pointing into the subdomain. M is the mass or energy per volume where $\kappa = 1,\ldots,$ NK, labeling the mass components such that NK is the total number of mass components and κ = NK+1 designates the heat component. **F** is the sum of mass or heat flux over phases, defined by equation 8 in this document, and q is a source and sink term.

For multiphase flow, TOUGH2 governs the flux of an individual phase by the equation

$$\mathbf{F}_{\beta} = \rho_{\beta}\mathbf{u}_{\beta} = -k\frac{k_{r\beta}\rho_{\beta}}{\mu_{\beta}}\left(\nabla P_{\beta} - \rho_{\beta}\mathbf{g}\right) \qquad (8)$$

where $\boldsymbol{u}_\beta$ is the Darcy velocity for a phase β, k is absolute permeability, $k_{r\beta}$ is the relative permeability for that phase, ρ_β is the phase density, μ_β is the phase viscosity, $\boldsymbol{g}$ is the acceleration due to gravity, and P_β is the fluid pressure for that phase. For the purposes of this model, the vertical migration of gaseous methane is the primary flux of interest, and the model domain was therefore designed as a column under hydrostatic conditions with no source or sink terms.

For multiphase flow, liquid and gas relative permeabilities were determined by the van Genuchten-Mualem model (Mualem, 1976; van Genuchten, 1980), such that

$$k_{rl} = \begin{cases} \sqrt{S^*}\left\{1 - \left(1 - [S^*]^{1/\lambda}\right)^{\lambda}\right\}^2 \; if \; S_l < S_{ls} \\ 1 \quad if \; S_l \geq S_{ls} \end{cases} \tag{9}$$

and

$$k_{rg} = \begin{cases} 1 - k_{rl} \; if \; S_{gr} = 0 \\ \left(1 - \hat{S}\right)^2\left(1 - \hat{S}^2\right) \; if \; S_{gr} > 0 \end{cases} \tag{10}$$

subject to the restriction $0 \leq k_{rl}, k_{rg} \leq 1$, and where S^* and $\hat{S}$ are defined as

$$S^* = (S_l - S_{lr})/(S_{ls} - S_{lr}) \tag{11}$$

$$\hat{S} = (S_l - S_{lr})/\left(1 - S_{lr} - S_{gr}\right) \tag{12}$$

Capillary pressure was determined by the corresponding van Genuchten function (van Genuchten, 1980), stated as

$$P_{cap} = -P_0\left([S^*]^{-1/\lambda} - 1\right)^{1-\lambda} \tag{13}$$

subject to the restriction $-P_{max} \leq P_{cap} \leq 0$, and for which S^* is defined in equation 11. For both the relative permeability and capillary pressure functions, S_l is liquid saturation, S_{lr} is residual liquid saturation, S_{ls} is the liquid saturation when k_{rl} is 1, S_{gr} is residual gas saturation, and λ is a fitting parameter defined by van Genuchten. P_0 is defined within TOUGH2 such that

$$1/P_0 = \alpha/\rho_w g \tag{14}$$

where α is a water retention parameter proportional to hydraulic conductivity. For both the relative permeability and capillary pressure functions, values for S_{lr}, λ, and α were taken from values presented for a sand in Carsel and Parrish, 1988. S_{gr} was set to 0.01, which was the lowest order of magnitude that resulted in a stable simulation.

Models in TOUGH2 were run using the EWASG (**WA**ter-**S**alt-**G**as) equation of state, which was designed for modeling geothermal reservoirs with saline fluids and non-condensible gas, and which was selected in this case because it allows for modeling of methane gas in particular. The primary variables incorporated by the EWASG module are pressure, salt mass fraction, non-condensible gas mass fraction or gas phase saturation, and temperature. For the purposes of this scenario, salinity was neglected and the salt mass fraction was considered to be zero for all models.

The model mesh created for this scenario is a simple 200 x 2530 meter grid, composed of 10 x 10 meter grid cells over a 10 meter thickness, representative of a 200 meter wide column extending from the surface to the base of the Elko Formation at the M2C-M2-21B well. This mesh was subdivided based on the formation thicknesses found

in the M2C-M2-21B well, and grid cells representing the Elko Formation were further subdivided to create a central section representative of the hydraulically fractured shale, while cells on either side represent the un-fractured shale (Figure 13a). A second model mesh was created using the same design, but with the addition of a transmissive 'fault zone,' represented by a vertical column of cells with increased hydraulic conductivity extending from the contact between the Elko and Indian Well Formations to the upper boundary layer (Figure 13b). Appropriate porosities, intrinsic permeabilities, and thermal conductivities were assigned to each formation, and hydraulic conductivities for the Indian Well Formation and fault were varied over a series of simulations (Table 6).

Table 6. Parameters for methane degassing simulations

Formation	Porosity	Permeability (m^2)	Thermal conductivity (W/m˚C)
Tertiary sediments	0.35	1.18e-12	2.0
Indian Well Formation	0.20	1.18e-13	1.7
Elko Formation	0.20	5.90e-16	2.9
Elko Formation (fractured)	0.20	5.90e-13	2.9
Fault zone	0.20	5.00e-12	2.1

Initial pressure and temperature conditions for the model were established by creating an upper boundary layer with a very small thickness but a very large volume and high specific heat, such that the temperature and pressure conditions prescribed for the cells in this layer would remain constant without being included in the balance equations for the model. The pressure within this layer was then set to atmospheric pressure (101.3 kPa) at a temperature of 15˚C and the model was run to steady state, creating a hydrostatic pressure gradient through the column. Using this pressure distribution as the initial condition for a second run to steady state conditions, the temperature at the lower

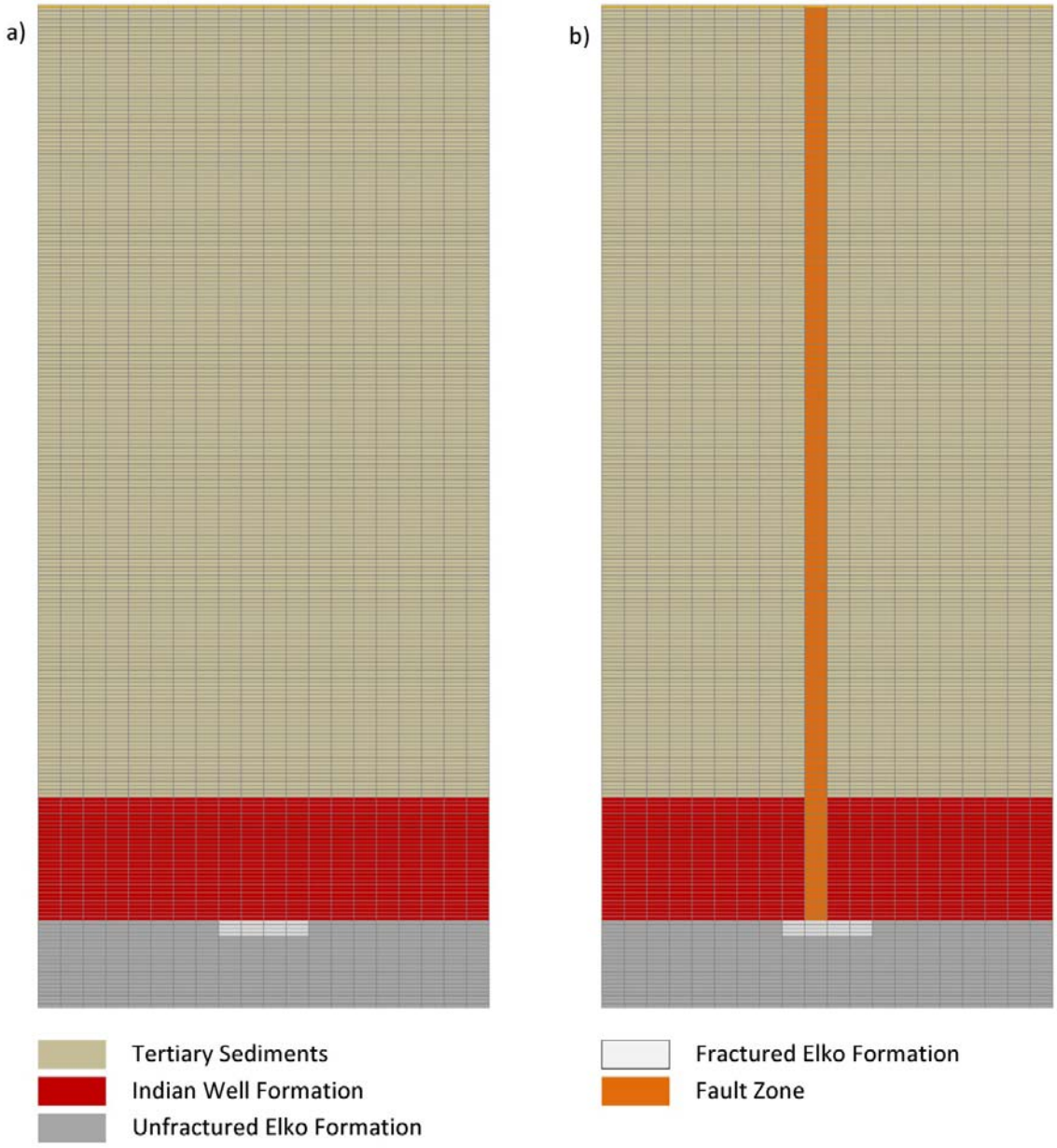

Figure 13. Model domains for methane degassing scenario in TOUGH2, 0.25 vertical exaggeration

boundary was then set to 80˚C and the model was set to perform a semi-analytical heat exchange, allowing heat to propagate to the surface and resulting in temperatures approximating a typical geothermal gradient. These models were run to steady state under fully saturated conditions, with no salinity and a ubiquitous mass fraction of dissolved methane of 1.0e-6.

The combination of these two model runs produced the pressure and temperature profile used in the initial conditions for the methane transport simulations. For the no-fault simulation, a 0.6 methane gas saturation (defined as the proportion of pore space occupied by a gas phase) was placed in all cells representing the fractured Elko Formation. For the fault simulations, methane gas saturations of 0.4, 0.5, and 0.6 were modeled over varying hydraulic conductivities of the fault zone and Indian Well Formation to determine sensitivity to these parameters (Table 7). Gas was then allowed to migrate and re-dissolve as dictated by pressure and temperature over a model period of 70 years.

Table 7. Parameters used for sensitivity analysis of methane degassing scenario

Simulation	IW Formation K (m^2)	Fault Zone K (m^2)	Initial Gas Saturation
1-Base Scenario	1.18e-13	5.00e-12	0.4
2-Base Scenario	1.18e-13	5.00e-12	0.5
3-Base Scenario	1.18e-13	5.00e-12	0.6
4-High K IW	2.36e-13	5.00e-12	0.4
5-High K IW	2.36e-13	5.00e-12	0.5
6-High K IW	2.36e-13	5.00e-12	0.6
7-High K Fault	1.18e-13	1.00e-11	0.4
8-High K Fault	1.18e-13	1.00e-11	0.5
9-High K Fault	1.18e-13	1.00e-11	0.6
10-No Fault Scenario	1.18e-13	n/a	0.6

RESULTS

Fractured Carbonate Scenario

Of the five sorption coefficients simulated, only three showed the potential for migration to a shallow water aquifer within 2000 years, though none allowed for migration of detectable concentrations. Not surprisingly, the use of lower sorption coefficients resulted in more rapid transport and higher peak concentrations. Models using the two highest sorption coefficients, representing hydrotreated light petroleum distillate (high sorption) and naphthalene (very high sorption), did not result in migration to the shallow water aquifer and showed very little migration even within the carbonate formation.

For the ethanol (very low sorption) simulations, the maximum concentration achieved in the aquifer was approximately 0.00052 mg/L, occurring after 554 years during Simulation 10, when the hydraulic conductivity of the metamorphic core complex was increased to 0.05 m/d. The most rapid migration occurred during Simulation 2, when the recharge flux was increased to 0.006 m/d. In this scenario, initial breakthrough occurred at 347 years, while concentrations in the aquifer peaked after 539 years. In all scenarios, dispersion along the carbonate flow path greatly reduced the maximum concentration of the plume, and peak concentration in the shallow water aquifer remained an order of magnitude below the normalized detection limit of 0.0043 mg/L. For each scenario, a breakthrough curve plotted for the node achieving the earliest breakthrough within the shallow aquifer (less than 600 feet below land surface) reveals how recharge, formation conductivity, and fault parameters control the time of transport to the surface

(Figure 14). Note that while these curves do not show the peak concentrations achieved for all simulations, peak concentrations were all on the same order of magnitude as the concentrations shown.

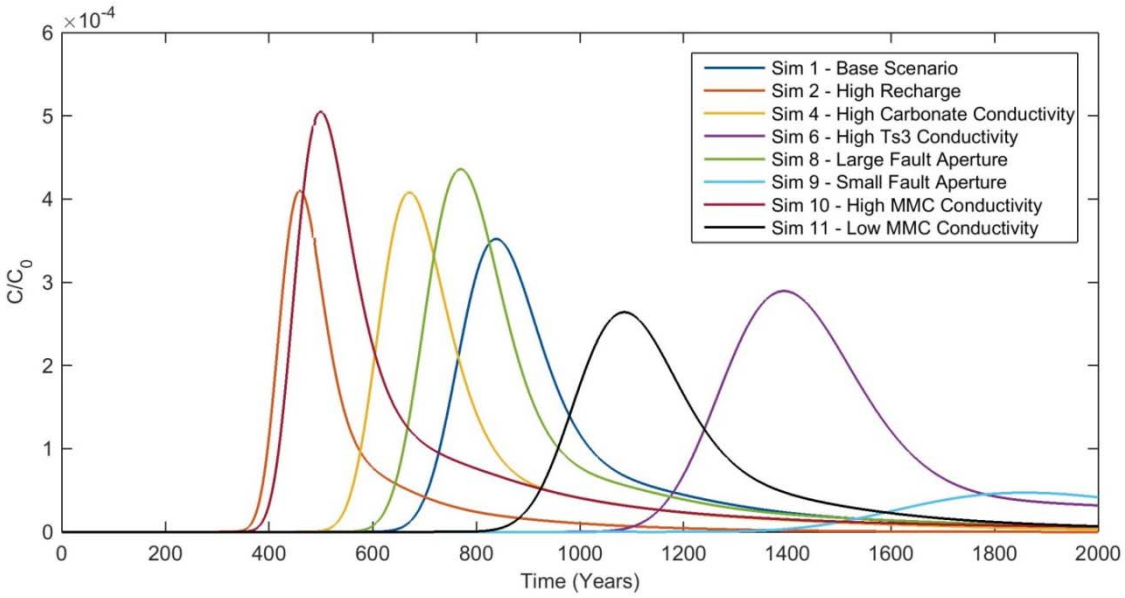

Figure 14. Breakthrough curves for fractured carbonate scenario using sorption parameters for ethanol (very low sorption)

A similar, though not identical trend can be seen in the fluid flux in the carbonate formation (Table 8). The magnitudes of the resultant fluxes correlate with the arrival times depicted in Figure 14 in all cases except for Simulations 2 and 10 (high recharge and high metamorphic core complex conductivity), where Simulation 2 shows more rapid transport despite a lower fluid flux.

Table 8. Darcy fluxes in the carbonate formation at the point of node of mass placement. Negative fluxes indicate flow downwards and to the left for the Y and X components, respectively.

	Darcy Flux in Carbonate Formation (m/d)		
Simulation	**X-component**	**Y-component**	**Resultant Flux**
Sim 1 - Base Scenario	-1.23E-03	-8.30E-05	1.23E-03
Sim 1 – Alt. Geologic Interpretation	-4.85E-03	-1.75E-04	4.85E-03
Sim 2 - High Recharge	-2.14E-03	-1.43E-04	2.14E-03
Sim 4 - High Carbonate Conductivity	-1.56E-03	-7.73E-05	1.56E-03
Sim 6 - High Ts3 Conductivity	-7.61E-04	-5.23E-05	7.62E-04
Sim 8 - Large Fault Aperture	-1.26E-03	-8.56E-05	1.26E-03
Sim 9 - Small Fault Aperture	-9.40E-04	-5.93E-05	9.42E-04
Sim 10 - High MMC Conductivity	-2.76E-03	-1.15E-04	2.76E-03
Sim 11 - Low MMC Conductivity	-7.80E-04	-7.15E-05	7.84E-04

For the ethylene glycol monobutyl ether (low sorption) simulations, the maximum concentration in the aquifer was approximately 0.0004 mg/L occurring after 945 years during Simulation 10, when the hydraulic conductivity of the metamorphic core complex was increased to 0.05 m/d. The most rapid transport also occurred during Simulation 10, with initial breakthrough occurring at 605 years (Figure 15). For all scenarios, peak concentrations remained an order of magnitude below the normalized detection limit of 0.0021 mg/L.

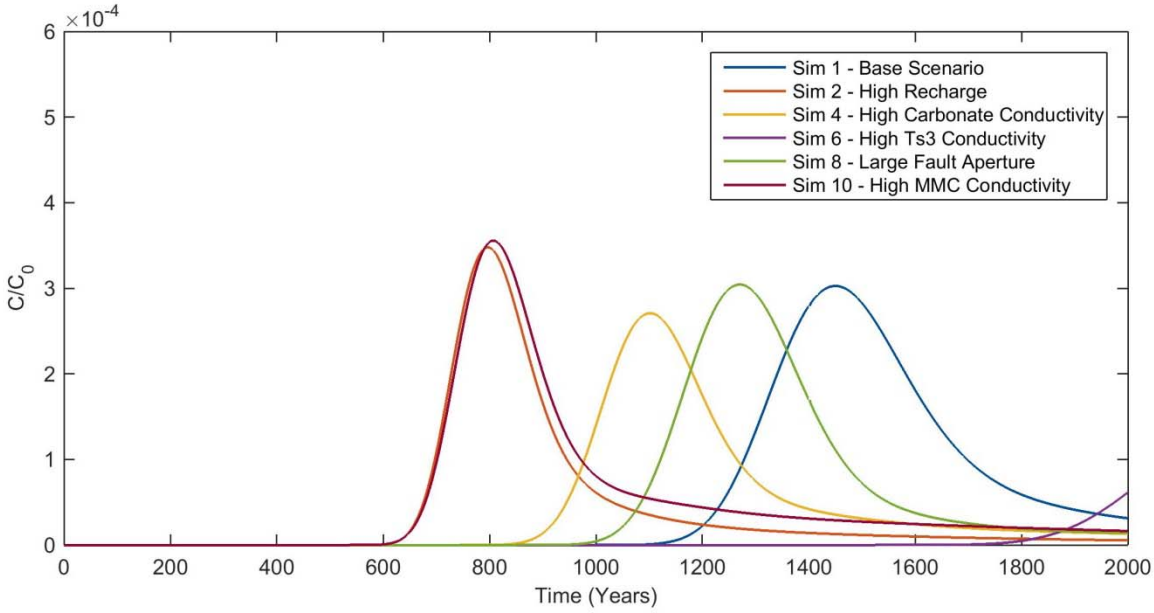

Figure 15. Breakthrough curves for fractured carbonate scenario using sorption parameters for ethylene glycol monobutyl ether (low sorption)

For the 2,2-dibromo-3-nitrilopropionamide (moderate sorption) simulations, the maximum concentration in the aquifer was approximately 0.00015 mg/L, occurring after 2000 years during Simulation 10, when the hydraulic conductivity of the metamorphic core complex was increased to 0.05 m/d. The most rapid migration occurred during Simulation 2, when the recharge flux was increased to 0.006 m/d. In this scenario, initial breakthrough occurred at 1533 years, while concentrations in the aquifer peaked after 1996 years (Figure 16). For all scenarios, peak concentrations remained 2 orders of magnitude below the normalized detection limit of 0.099 mg/l.

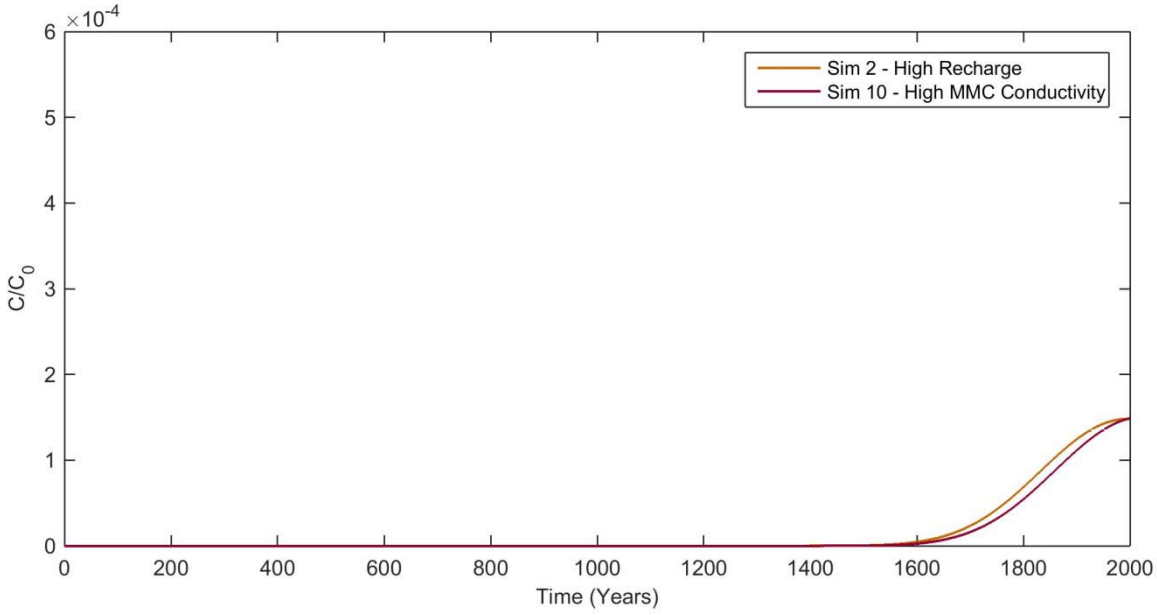

Figure 16. Breakthrough curves for fractured carbonate scenario using sorption parameters for 2,2-dibromo-3-nitrilopropionamide (moderate sorption)

By far, the most rapid arrival time occurs with the simulation using the alternative geologic interpretation. Using sorption parameters for ethanol, initial breakthrough occurs at 231 years, with a peak concentration of 0.00051 mg/l occurring after 316 years. Though the hydrologic parameters used for this simulation are the same as those used in the base simulation, the result is a time shift of approximately 60% between breakthrough curves (Figure 17). However, the peak concentrations for these two simulations are on the same order of magnitude.

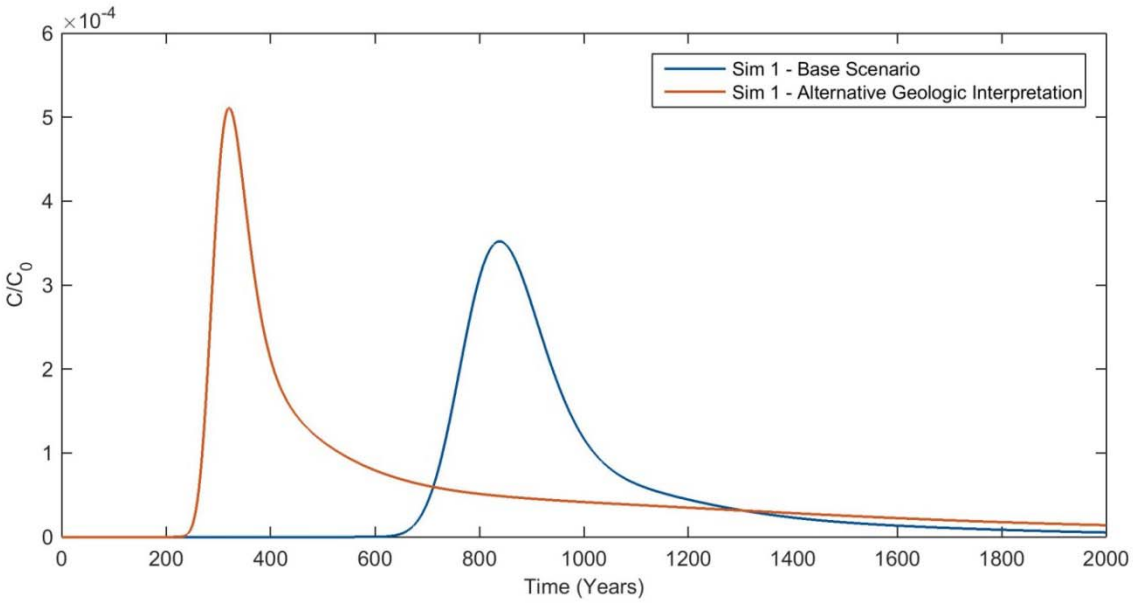

Figure 17. Breakthrough curves for the fractured carbonate scenario comparing results of the base scenario to those using the alternative geological interpretation.

Fault Connectivity Scenario

As described for the fractured carbonate scenario, any simulation showing a concentration greater than 0.0043 mg/L within the upper 600 feet of the model domain (i.e., the shallow water aquifer) would be indicative of a scenario allowing contaminant migration – however, for this scenario, none of the nine simulations showed any concentration present in the shallow water aquifer after a period of 2000 years. For all simulations, vertical transport through the fault did not occur and the majority of the tracer was instead transported laterally through the Indian Well Formation, with the exception of Simulation 2 (Figure 18). Here, the tracer was transported downward through the Elko Formation and into the underlying carbonate formation, where it was

then transported laterally. In the case of scenario 3, where the hydraulic conductivity of the Indian Well Formation was greatly increased, a lateral migration through that formation occurred similar to what was seen in the fractured carbonate scenario discussed in the previous section. However, it is extremely unlikely that that conductivity would be valid for anything beyond a locally fractured welded tuff, and these results were considered an effective impossibility and therefore not analyzed further. None of the variations created the conditions necessary to transport the contaminant mass near the shallow water aquifer.

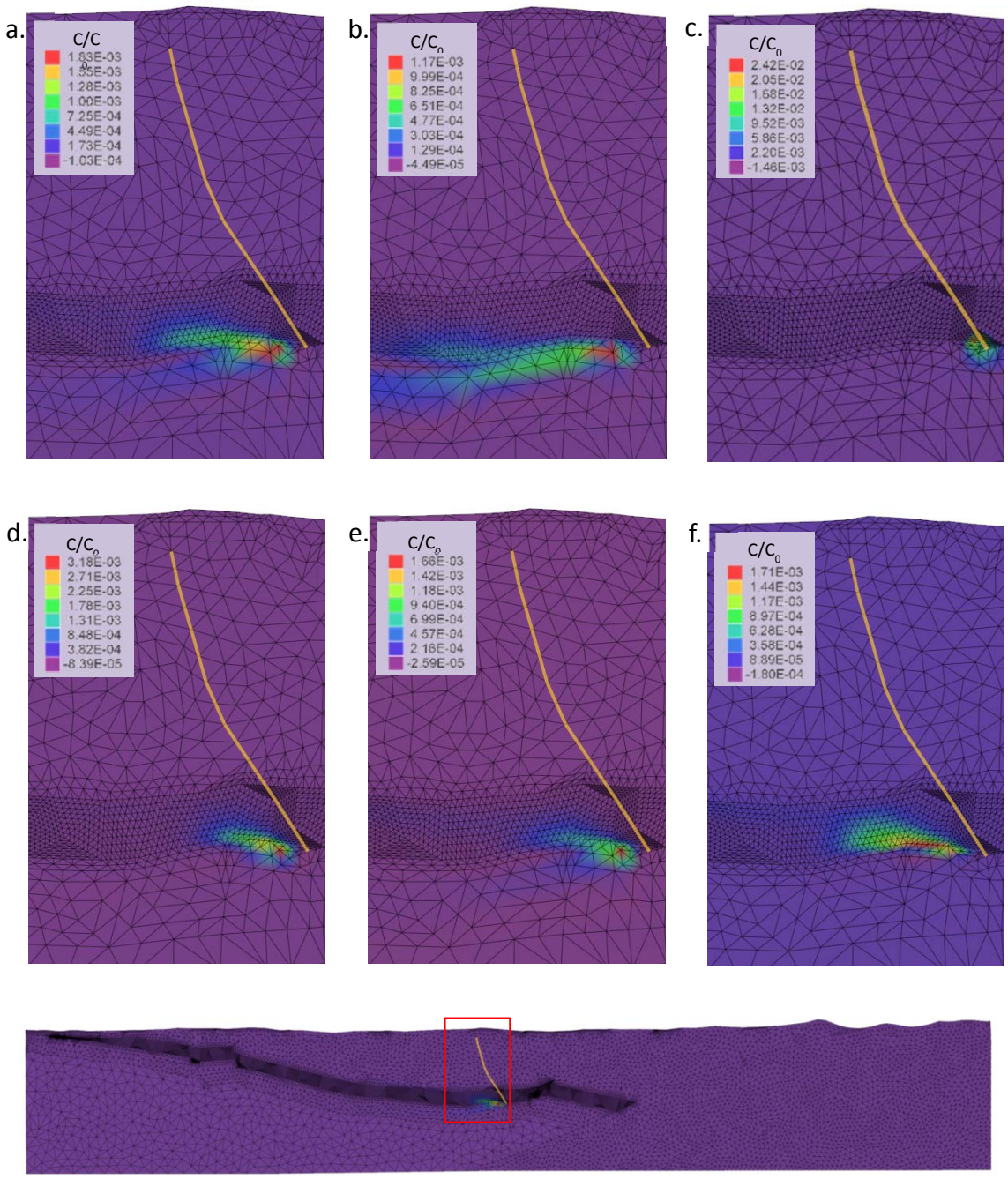

Figure 18. Results of fault connectivity simulations with relevant area magnified from full model domain. a) Simulation 1 - Base model; b) Simulation 2 – Recharge = 0.06 m/d; c) Simulation 4 – Indian Well K = 0.0001 m/d; d) Simulation 5 – Ts3 K = 2 m/d; e) Simulation 6 – Fault aperture = 0.01 m; f) Simulation 7 – MMC K = 0.05 m/d. Simulation 3 not pictured. Fault trace shown in yellow.

Methane Degassing Scenario

Of the ten scenarios tested, none showed the potential for transport to a shallow water aquifer (less than 600 feet below land surface) within 70 years (Figure 19). The greatest vertical distances traveled occurred when the initial gas saturation was increased to 0.6, with gas in the base scenario traveling a total of 1870 meters (6135 feet) and reaching a depth of 455 meters (1493 feet) below the surface. The shortest vertical distances traveled resulted when the initial gas saturation was decreased to 0.4, with gas in the base scenario traveling a total of 800 meters (2625 feet) and reaching a depth of 1525 meters (5003 feet) below the surface.

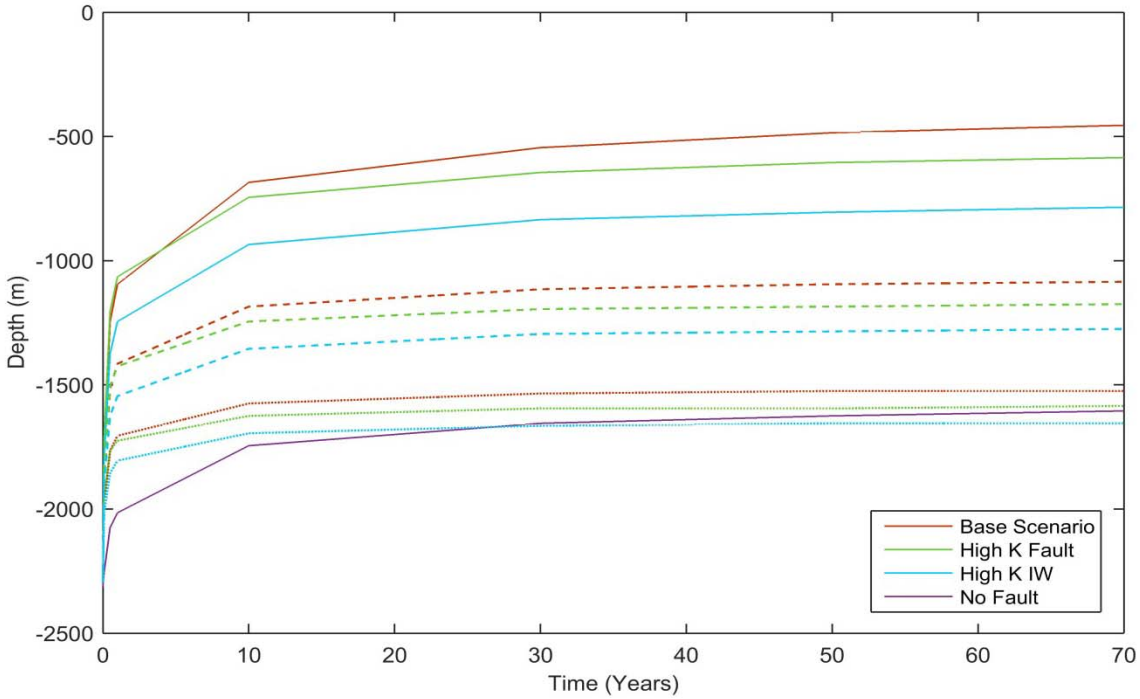

Figure 19. Depth to upper boundary of methane gas plume for initial $S_g = 0.6$ (solid line), $S_g = 0.5$ (dashed line), and $S_g = 0.4$ (dotted line)

The spatial distribution of methane gas saturation follows the same general pattern for all fault zone scenarios, with the majority of migration occurring vertically through the fault zone, a lesser degree of vertical migration through the Indian Well Formation, and minor or negligible lateral spreading. The spatial distribution for each time step in the scenario showing the greatest migration (Base Scenario, $S_g = 0.6$), is shown here in Figure 20. Spatial distributions of methane gas saturation for all other fault zone scenarios can be found in Appendix C. While the spatial distribution of methane gas saturation for the no-fault scenario is also indicative of dominant vertical migration, this scenario results in significantly more lateral spreading in the Indian Well Formation (Figure 21).

For each initial gas saturation tested, the greatest migration resulted from the parameters set in the base scenario, followed by the high permeability fault scenario, and lastly by the high permeability Indian Well scenario. Interestingly, migration is initially more rapid for the high permeability fault scenarios than for the base scenarios, though for all initial gas saturations the total distance migrated in the base scenarios overtakes that of the high permeability fault scenarios within the first five years. For all scenarios, with the exception of the no-fault scenario, over 87% of the total migration distance is traveled within the first 10 years of migration, and over 95% is traveled within the first 30 years, as gas saturations approach the prescribed residual gas saturation of 0.01 and the gas is immobilized.

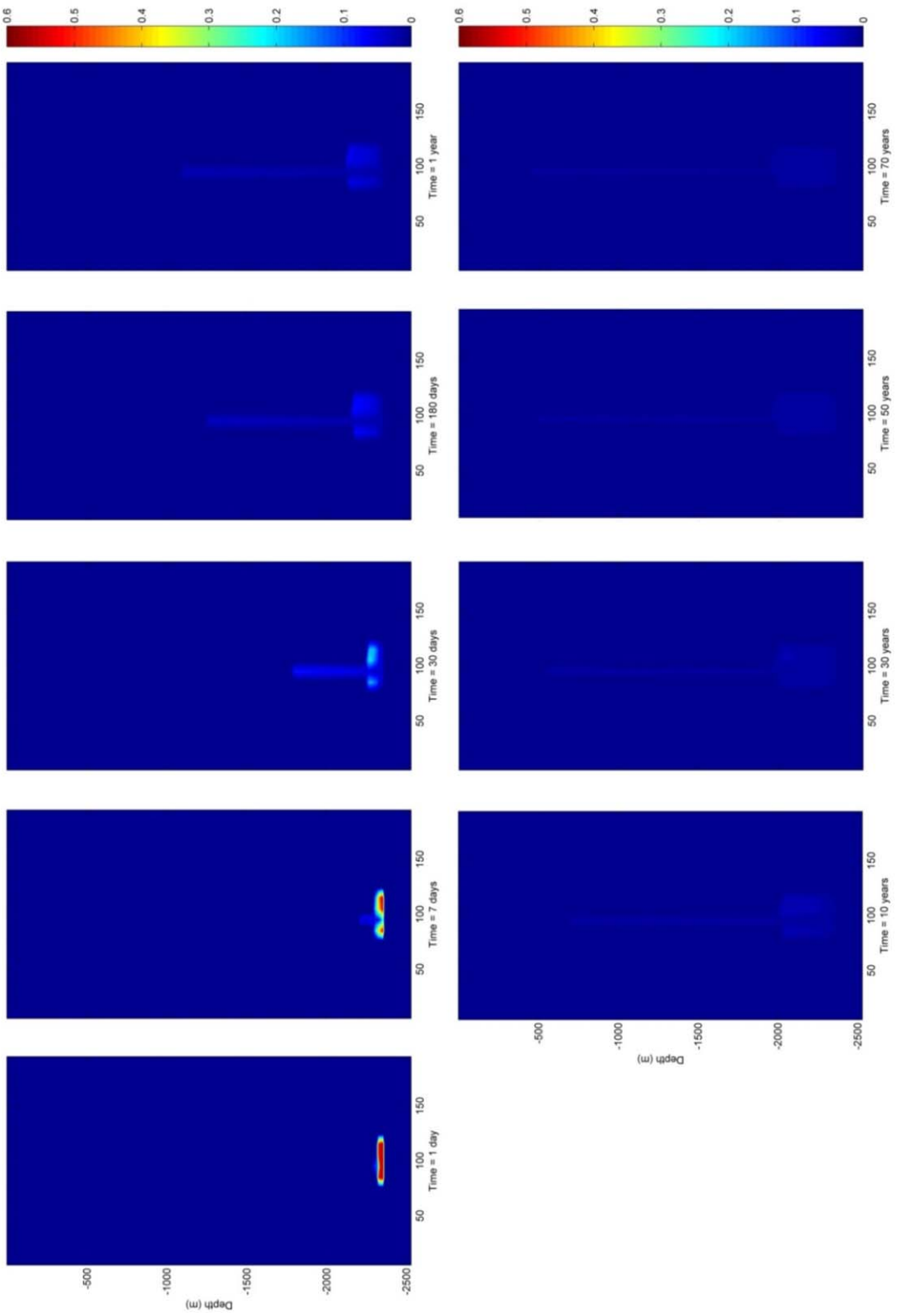

Figure 20. Methane gas saturation for Base Scenario, Sg = 0.6

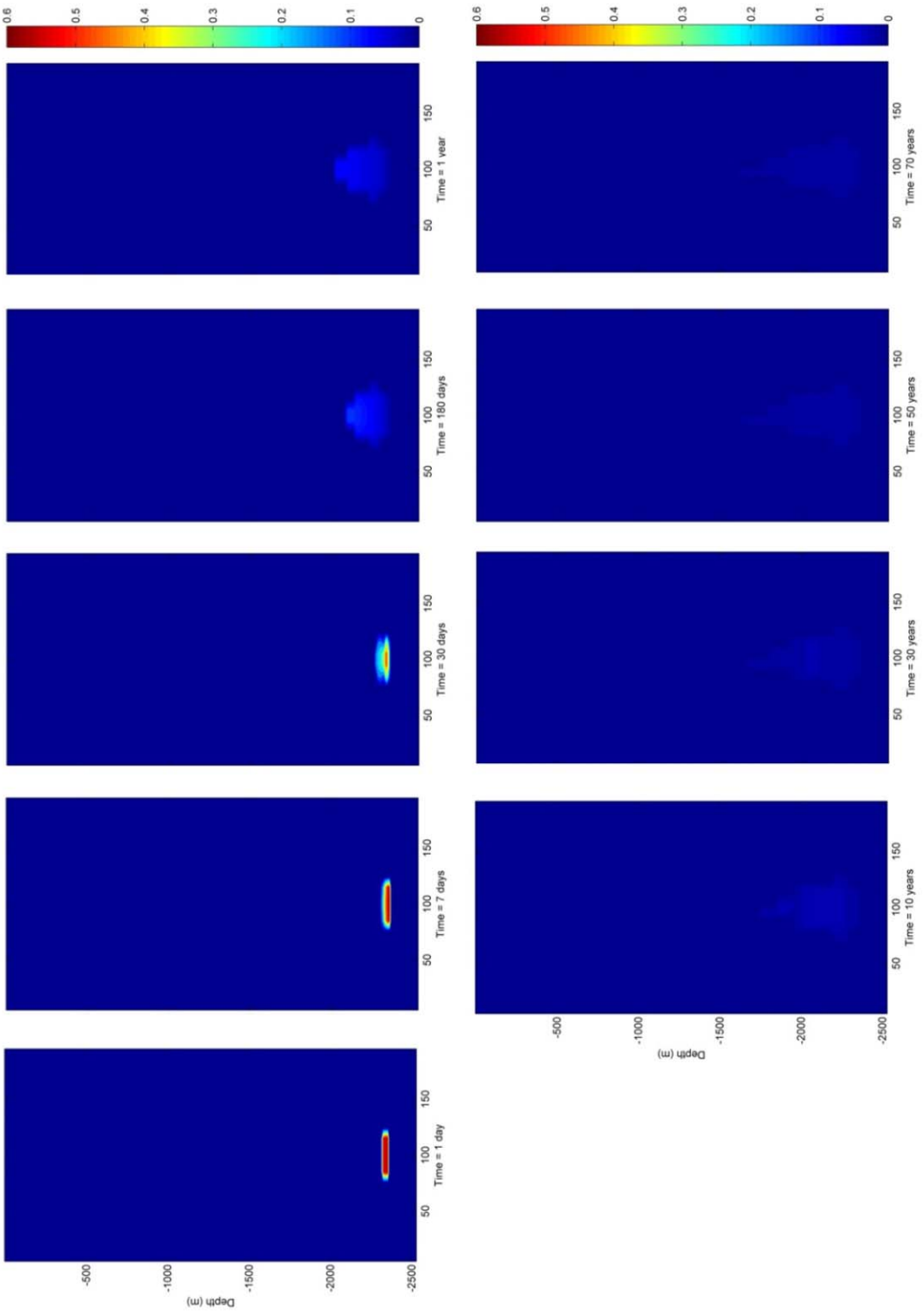

Figure 21. Methane gas saturation for no-fault scenario

DISCUSSION

Fractured Carbonate Scenario

Direct comparison between the breakthrough curves of the various combinations of constituents and model conditions is difficult because the breakthrough curves are representative of the model node in the shallow water aquifer achieving the most rapid breakthrough, which was not the same node in all cases. In all cases, these nodes were located near the upper terminus of the fault, however, some breakthrough curves are representative of nodes further downstream than others, meaning that the plume will have had more opportunities to sorb before breaking through the lower boundary of the shallow water aquifer. The breakthrough curves were not plotted at the same node for all scenarios because in many cases this implied that no migration had occurred at all, when in fact breakthrough was occurring at a node 30-300 meters downstream.

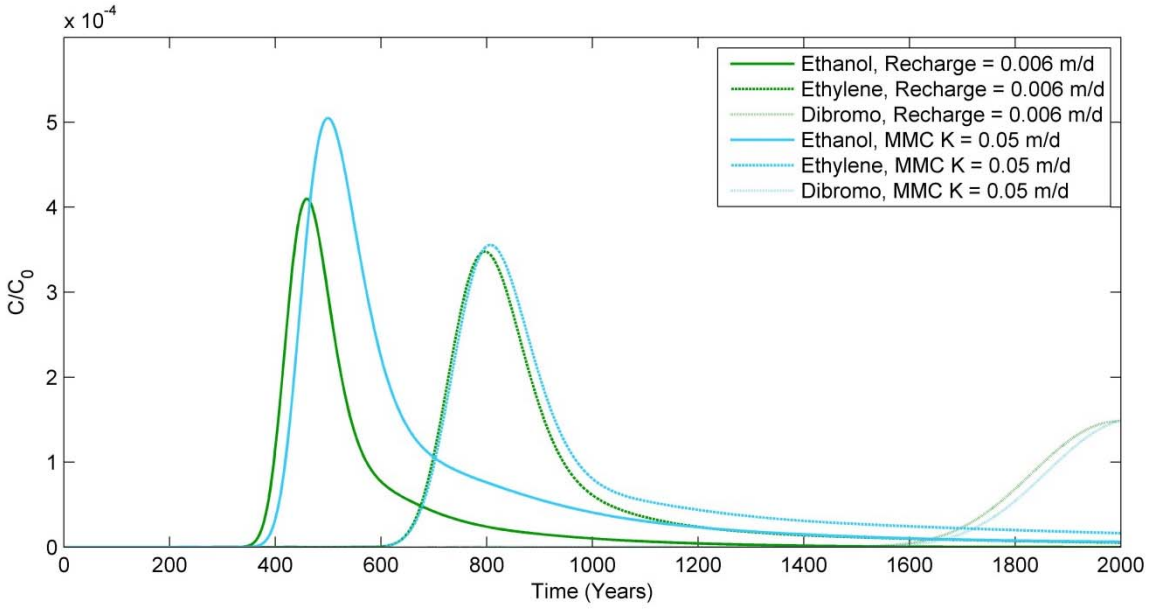

Figure 22. Comparison of breakthrough curves for scenarios showing the most rapid transport for three sorption parameters

Despite this, some general comparative observations can be made. The three constituents show the roughly the same order of arrival time and peak concentration among the eleven scenarios. An increase in the sorption coefficient results in a delayed arrival time, a decrease in peak concentration, and an increase in constituent residence time (Figure 22). For all constituents, increased recharge, increased hydraulic conductivity of the carbonate formation and the metamorphic core complex, and an increased fault aperture resulted in greater peak concentrations and earlier arrival times relative to the base scenario, which was not unexpected given the increased flow velocities resulting from these conditions.

Interestingly, for all constituents, an increase in the hydraulic conductivity of the Tertiary sediments results in less rapid transport than the base scenario, and a depleted peak concentration. This occurs because model recharge occurs over both the Tertiary sediments and the metamorphic core complex (as well as the carbonate outcrop, which is then diverted into one of these two formations). When the hydraulic conductivity of the sediments is increased, recharge flows preferentially through the sediments and bypasses the lower conductivity metamorphic core complex, which acts as the main conduit of flow to the carbonate formation. This also occurs when the hydraulic conductivity of the metamorphic core complex is decreased relative to that of the Tertiary sediments – in either case, the carbonate formation receives less recharge, and the fluid velocity is decreased.

Similarly, the highest fluid fluxes are seen in the carbonate formation for the increased metamorphic core complex conductivity scenario (Table 8), while this scenario

shows slightly delayed transport relative to the high recharge scenario for all sorption parameters (Figures 14, 15, 16). These results show that while arrival times are strongly correlated with the ability of the system to transport fluid through the carbonate formation, fluxes through other formations, particularly the Tertiary sediments, also play a role.

A reduction of the fault aperture not only results in a greatly delayed arrival time, but in a large decrease in the peak concentration as well. Within the model domain, there is a 'fork' in the flow regime, such that fluid may migrate upwards through the fault or remain in the carbonate formation and continue flowing westward. While all scenarios show some flux through the carbonate formation, when the fault aperture is decreased the carbonate formation becomes the dominant flow path, and the majority of the constituent mass remains in that formation.

The model design used here is highly conservative, and does not consider a number of factors which could slow or halt constituent transport. Firstly, the model assumes direct injection of fracking fluid into the carbonate formation. However, application of the volume of water injected to the equation derived by Flewelling et al., 2013, indicates that there is only a 5% chance that fracture lengths could extend into that formation. A more likely scenario for constituent entry into this formation would be via downward advection through the overlying shale formation, which would increase the overall time to breakthrough and decrease the peak concentration. Additionally, the effect of pumping is not considered, which would create a local gradient in the direction of the well and further delay migration until such time that pumping ceased. The model also

assumes no chemical breakdown, biodegradation, or interactions between chemicals, all of which would reduce peak breakthrough concentrations.

Perhaps most importantly, the model assumes the existence of a conductive fault connecting the carbonate formation to the overlying Tertiary sediments. While the study area is known to be faulted, the exact locations of these faults are not known, nor are their vertical extents or conductivities – faults may also act as barriers to flow. However, without a continuous, conductive fault, transport to a shallow water aquifer would not be possible.

Fault Connectivity Scenario

Though none of the tested simulations produced the conditions necessary to transport the contaminant mass to a shallow water aquifer, variation of fault parameters, system recharge, and formation conductivities did affect the preferential flow path for migration, though none promoted vertical migration through the fault zone.

In general, scenario parameters resulting in an increased fluid flux through the Indian Well Formation resulted in increased lateral transport relative to the base scenario. These scenarios include increased recharge, increased hydraulic conductivity of the Indian Well Formation, and increased hydraulic conductivity of the metamorphic core complex. Scenario parameters resulting in a decreased fluid flux through the Indian Well Formation showed decreased lateral transport. These scenarios include decreased hydraulic conductivity of the Indian Well Formation, and increased hydraulic conductivity of the overlying Tertiary sediments, which allowed additional recharge to

flow through that formation, bypassing the Indian Well. An increased fault aperture did not create a preferential flow path through the fault, as the local gradient remained generally downward.

As in the fractured carbonate scenario, the presence of a continuous, connective fault is unknown and assumed. Because initial simulations did not result in significant transport, additional simulations including sorption parameters were not tested, nor were the effects of chemical breakdown, biodegradation, or chemical interactions considered. As in the fractured carbonate flow simulations, the effects of pumping the oil well were also not considered. All of these factors would serve to further retard or eliminate the already insignificant transport shown in these simulations.

Methane Degassing Scenario

Though none of the simulations tested produced the conditions to transport gaseous methane to the shallow water aquifer, several did result in significant migration. Migration is heavily controlled by the initial gas saturation in the fractured oil shale, the presence of a continuous, conductive fault, and to a lesser extent, the permeability of the Indian Well Formation.

In the case of increased permeability of the Indian Well Formation, the fault zone remains the primary migration pathway, but the rate of vertical migration through the Indian Well Formation increases at the expense of migration through the fault zone. Gaseous methane that might otherwise migrate laterally to connect with the conductive fault instead migrates vertically, decreasing the total volume of gas in the fault zone.

For both the base scenario and the high permeability fault scenario, the fault zone is the primary migration pathway. Interestingly, methane gas travels a greater vertical distance in the base scenario than in the high permeability fault scenario for all three tested initial gas saturations. In each case, gas initially migrates more rapidly in the high permeability fault scenario than in the base scenario, but is overtaken by the rate of migration in the base scenario within the first five years. This occurs because relative permeability is a function of gas saturation as described in Equations 10 and 12, and the high permeability fault scenario results in a consistently lower gas saturation relative to the base scenario within the fault for each time step. Initially, the difference in gas saturations is small and the increased absolute permeability in the high permeability fault scenario compensates for the decreased relative permeability factor. As the difference in gas saturations between the two scenarios widens, the relative gas permeability in the base scenario fault zone exceeds that of the high permeability fault scenario (Figure 22).

The model design used here is both conservative and simplistic. While a no-fault scenario was also tested, the presence of a continuous, vertical, conductive fault zone directly overlying the frack zone is clearly improbable and was used only to allow a better analysis of the factors that might contribute to increased gas migration. The model also assumed a column under hydrostatic conditions. Realistically, a natural downward or lateral groundwater flux would result in spreading in those directions and a resultant decrease in upwards vertical migration. Similarly, while an initially decreased formation pressure due to pumping is a condition for this scenario, the effects of continuous

pumping were not considered, and formation pressure was allowed to return to hydrostatic.

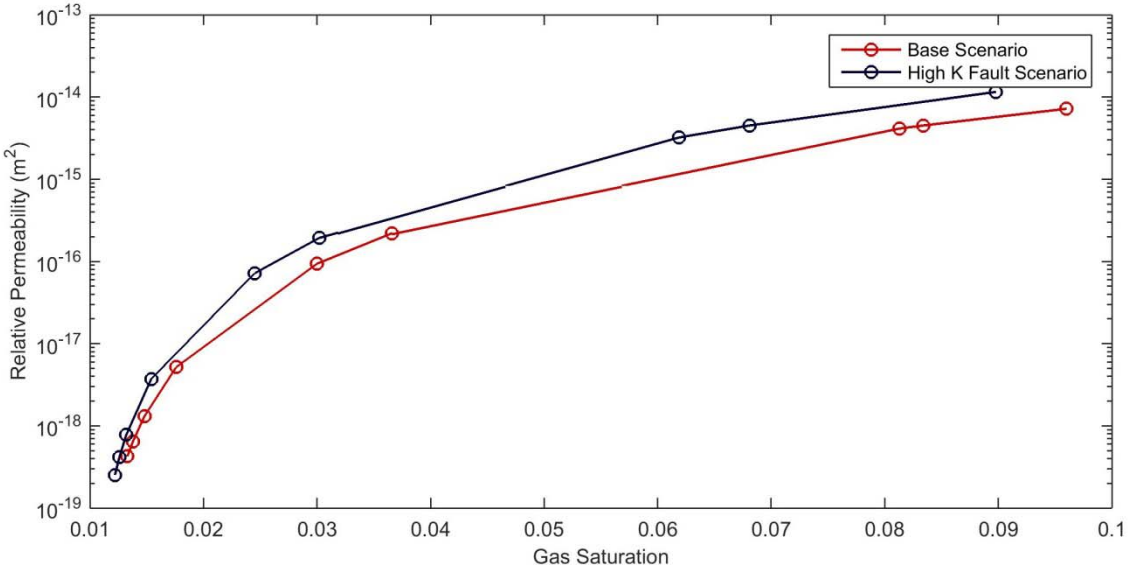

Figure 23. Relative gas permeability for gas saturation at head of plume, initial $S_g = 0.6$.

It should also be noted that the initial gas saturations tested in these models are not the only potential values, as the dissolved methane concentration in the Elko shale is not known. The inclusion of other gases which would likely be present, such as ethane, propane, and carbon dioxide, was also not considered, nor was salinity, all of which would reduce the solubility of methane gas.

CONCLUSIONS

Results indicate that migration of detectable concentrations is extremely unlikely, and of the three migration scenarios tested, only the fractured carbonate scenario showed potential for *any* transport to a shallow water aquifer on a timescale of concern (< 2000 years). These simulations show that any migration would be of concentrations several orders of magnitude below detectable limits, and would be dependent on a number of very specific conditions. For migration of fracking fluids, these conditions include 1) hydraulic fractures connecting the Elko shale with the adjacent carbonate formation, 2) the presence of a continuous, conductive fault connecting the adjacent carbonate formation with an overlying shallow water aquifer, 3) significant mountain block recharge in the Ruby Mountains, 4) carbonate hydraulic conductivity at a minimum of 0.1-1 m/d, 5) metamorphic core complex hydraulic conductivity on the order of 0.005 m/d or higher, and 6) fracking fluid constituents with very low to moderate sorption parameters.

It should be stressed that all of these conditions must be fulfilled in order for any migration to occur on a meaningful timescale, and the likelihood of that scenario is unknown. Models were designed with these conditions in place as a method for testing the *only* apparent flow path for migration. It should also be stressed that these simulations only indicate the potential for migration of concentrations several orders of magnitude below detection limits. While none of the constituents currently used in fracking fluids in the upper Humboldt Basin have a defined MCL (maximum contaminant level), any such level would likely be greater than the detection limit.

While the work described in this document does not indicate any significant hazard to local water quality, model designs are specific to one basin in particular, and the results are not necessarily transferable to other hydraulic fracturing sites. Given the results shown in the fractured carbonate and methane degassing scenarios, an individual risk assessment for any basin to be fracked should be undertaken, particularly for those with targeted shale deposits shallower than that depicted in these simulations.

This study attempted to assess the risk of hydraulic fracturing assuming a natural flow regime and disregarding the potential for well construction issues. As previous studies have indicated that poor well construction is the most likely scenario which would allow migration of fracking fluids or formation gases (Watson and Bachu, 2009), and because the risk of migration along a natural flow path appears to be extremely low, regulatory emphasis should be placed on well construction in this area.

REFERENCES

Anna, L. O., Roberts, L. N. R., and Potter, C. J. (2007). Geologic assessment of undiscovered oil and gas in the Paleozoic-Tertiary composite total petroleum system of the Eastern Great Basin, Nevada and Utah. *USGS Digital Data Series*, *DDS-69-L*, 55 p.

Beardsmore, G.R. and Cull, J.P. (2001). *Crustal Heat Flow. A Guide to Measurement and Modelling*. Cambridge University Press, 319 p.

Carsel, R. F., and Parrish, R.S. (1988), Developing joint probability distributions of soil water retention characteristics, *Water Resour. Res*., 24(5), 755–769, doi:10.1029/WR024i005p00755

Carter, K.M., Kresic, N., Muller, P., and Vittorio, L.F. (2013). Technical Rebuttal to Article Claiming a Link between Hydraulic Fracturing and Groundwater Contamination: Pennsylvania Council of Professional Geologists and the Pennsylvania Geological Survey.

Coats, R.R. (1987). Geology of Elko County, Nevada: Nevada Bureau of Mines and Geology Bulletin 101, p. 112, scale 1:250,000.

Cohen, H. A., Parratt, T. and Andrews, C. B. (2013). Potential contaminant pathways from hydraulically fractured shale to aquifers. *Groundwater*, 51: 317–319. doi: 10.1111/gwat.12015

Coolbaugh , M., Zehner, R., Kreemer, C., Blackwell, D.D., and Oppliger, G.L. (2005). A map of geothermal potential for the Great Basin, USA: Recognition of multiple geothermal environments. Geothermal Resources Council Transactions, v. 29

Davies, R. J., Mathias, S.A., Moss, J., Hustoft, S., and Newport, L. (2012). Hydraulic fractures: How far can they go? *Marine and Petroleum Geology*, *37*(1), 1–6. doi:10.1016/j.marpetgeo.2012.04.001

Diersch, Hans-Jörg (2014). *FEFLOW (Version 6.2) [Computer program]. DHI-WASY, Berlin, Germany.*

Eakin, T.E. and Lamke, R.D. (1966). Hydrologic Reconnaissance of the Humboldt River Basin, Nevada: State of Nevada Department of Conservation and Natural Resources and the U.S. Geological Survey, Water Resources Bulletin No. 32.

Epstein, B.J. (2004). Development and Uncertainty Analysis of Empirical Recharge Prediction Models for Nevada's Desert Basins. Hydrologic Sciences Program, University of Nevada, Reno, Master's Thesis.

Fetter, C.W. (1999). *Contaminant Hydrogeology*. Prentice-Hall, Inc. New Jersey, p. 500.

Flewelling, S.A., Tymchak, M.P., and Warpinski, N. (2013). Hydraulic fracture height limits and fault interactions in tight oil and gas formations. *Geophysical Research Letters*, *40*(14), 3602–3606. doi:10.1002/grl.50707

Frac Focus. (2013). What Chemicals are Used, Accessed April 12, 2013, http://fracfocus.org/chemical-use/what-chemicals-are-used.

Gassiat, C., Gleeson, T., Lefebvre, R., and McKenzie, J. (2013). Hydraulic fracturing in faulted sedimentary basins: Numerical simulation of potential contamination of shallow aquifers over long time scales. *Water Resources Research*, *49*(12), 8310–8327.

Hess, R.H., Henson, M.A., Davis, D.A., Limerick, S.H., Siewe, S.S., and Niles, M. (2011) Oil and gas well information for Nevada - 2011 update: Nevada Bureau of Mines and Geology Open-File Report 11-6.

Jackson, R. B., Vengosh, A., Darrah, T. H., Warner, N. R., Down, A., Poreda, R. J., Osborn, S.G., Zhao, K. and Karr, J. D. (2013). Increased stray gas abundance in a subset of drinking water wells near Marcellus shale gas extraction. *Proceedings of the National Academy of Sciences of the United States of America*, *110*(28), 11250–5.

Ketner, K.B. (1990). Geologic map of the Elko Hills, Elko County, Nevada: U.S. Geological Survey Miscellaneous Geologic Investigations Series Map I-2082, scale 1:24,000.

Kissinger, A., Helmig, R., Ebigbo, A., Class, H., Lange, T., Sauter, M., and Jahnke, W. (2013). Hydraulic fracturing in unconventional gas reservoirs: risks in the geological system, part 2. *Environmental Earth Sciences*, *70*(8), 3855–3873. doi:10.1007/s12665-013-2578-6

Masbruch, M.D. (2011a). Appendix 4: Current Study Groundwater Recharge Estimates for Predevelopment Conditions and Ranges of Previously Reported Estimates of Groundwater Recharge for Each Hydrographic Area within the Great Basin Carbonate and Alluvial Aquifer System Study Area. In: Conceptual Model of the Great Basin Carbonate and Alluvial Aquifer System. V.M. Heilweil and L.E. Brookes (Eds.). U.S Geological Survey Scientific Investigations Report 2010-5193.

Masbruch, M.D. (2011b). Appendix 5: Current Study Groundwater Discharge Estimates for Predevelopment Conditions and Ranges of Previously Reported Estimates of

Groundwater Discharge for Each Hydrographic Area within the Great Basin Carbonate and Alluvial Aquifer System Study Area. In: Conceptual Model of the Great Basin Carbonate and Alluvial Aquifer System. V.M. Heilweil and L.E. Brookes (Eds.). U.S Geological Survey Scientific Investigations Report 2010-5193.

Maxey, G.B. and Eakin, T.E. (1949). Ground water in White River Valley, White Pine, Nye, and Lincoln Counties, Nevada. No. 8, State of Nevada Office of the State Engineer prepared in cooperation with the United State Department of the Interior Geological Survey, Carson City, Nevada.

Mualem, Y. (1976). A new model for predicting the hydraulic conductivity of unsaturated porous media, *Water Resour. Res*., Vol. 12, No. 3, p. 513-522.

Myers, T. (2012). Potential contaminant pathways from hydraulically fractured shale to aquifers. *Groundwater*, *50*(6), 872–882.

Nevada Division of Minerals. (2014). Hydraulic fracturing in Nevada: History, current use, development of regulations and schedule for adoption, June 10, 2014. http://minerals.nv.gov

Plume, R. (1996). Hydrogeologic Framework of the Great Basin Region of Nevada, Utah and Adjacent States. *U.S. Geological Survey Professional Paper 1409-B*.

Plume, R. (2009). Hydrogeologic Framework and Occurrence and Movement of Ground Water in the Upper Humboldt River Basin , Northeastern Nevada Scientific Investigations Report 2009 – 5014.

Pohll, G., Chapman, J., Pohlmann, K., Plume, R., Parashar, R., Rybarski, S., Hershey, R., Fereday, W., Reeves, M., and Thomas, J. (2015). Assessment of the migration potential of hydraulic fracturing fluids in the Upper Humboldt River Basin, Nevada.

Prudic, D. E., Harrill, J. R., and Burbey, T. J. (1995). Conceptual evaluation of regional ground-water flow in the carbonate-rock province of the Great Basin, Nevada, Utah, and adjacent states. *U.S. Geological Survey Professional Paper 1409-D*.

Pruess, K., Oldenburg, C., and Moridis, G. (2012). *TOUGH2* (Version 2.1) [Computer program]. Earth Sciences Division, Lawrence Berkeley National Laboratory, University of California, Berkeley, California.

Rush, F.E. and Everett, D.E. (1966). Water Resources Appraisal of the Huntington Valley Area, Elko and White Pine Counties, Nevada: Nevada Department of Conservation and Natural Resources Water Resources Reconnaissance Series, Report 35.

Saiers, J. E. and Barth, E. (2012). Potential contaminant pathways from hydraulically fractured shale aquifers. *Groundwater*, 50: 826–828. doi: 10.1111/j.1745-6584.2012.00990.x

United States Environmental Protection Agency (2012). Study of the Potential Impacts of Hydraulic Fracturing on Drinking Water Resources: Progress Report.

Van Genuchten, M.Th. (1980). A closed-form equation for predicting the hydraulic conductivity of unsaturated soils, *Soil Sci. Soc*., Vol. 44, p. 892-898.

Vengosh, A., Warner, N., Jackson, R., and Darrah, T. (2013). The effects of shale gas exploration and hydraulic fracturing on the quality of water resources in the United States. *Procedia Earth and Planetary Science*, *7*, 863–866.

Water for Nevada, Nevada's Water Resources: State of Nevada Water Planning Report, Report No. 3, State Engineer's Office, 1971, p. 97.

Watson, T. and Bachu, S. (2009). Evaluation of the potential for gas and CO2 leakage along wellbores. *SPE Drill. Complet.,* 21(1), p. 115-126.

Zheng, C. and Bennett, G.D. (2002). *Applied Contaminant Transport Modeling*, 2nd ed. New York: John Wiley & Sons.

APPENDIX A

Well logs used in interpolation of basin geometry

Map ID	API	Elevation (ft)	TD (ft)	Depth of top (ft)	Hydrologic Units Penetrated	Stratigraphic Unit Penetrated
1	27-007-05003	5308	7349	0	Younger basin-fill deposits	
				909	Older basin-fill deposits	
				1152	Volcanic rocks	
				2386	Older basin-fill deposits	Humboldt Formation
				3002	Older basin-fill deposits	Elko Formation
				3903	Upper Paleozoic carbonates	
				5600	Mississippian clastic rocks	Chainman Formation
2	27-007-05004	5250	4125	0	Older basin-fill deposits	
				3150	Upper Paleozoic carbonates	Ely Limestone
				3630	Mississippian clastic rocks	White Pine Shale
3	27-007-05006	5505	5465	0	Younger basin-fill deposits	
				370	Older basin-fill deposits	
				3310	Mississippian clastic rocks	Chainman Shale
				4530	Lower Paleozoic carbonates	
4	27-007-05007	5589	8416	0	Older basin-fill deposits	
				8033	Lower Paleozoic carbonates	
				8380	Crystalline rocks	
5	27-007-05010	5973	6612	0	Younger basin-fill deposits	
				95	Older basin-fill deposits	
				2405	Volcanic rocks	
				6475	Crystalline rocks	Ordovician Kinnikinnic Quartzite
6	27-007-05208	6050	7106	0	Older basin-fill deposits	Humboldt Formation
				1690	Volcanic rocks	
				2800	Older basin-fill deposits	Elko Formation
				4230	Clastic sedimentary rocks	
7	27-007-05209	5182	5670	0	Older basin-fill deposits	Humboldt Formation
				3420	Volcanic rocks	
				4320	Older basin-fill deposits	Elko Formation
				5490	Upper Paleozoic carbonates	Ely Limestone
8	27-007-05213	5488	8714	0	Younger basin-fill deposits	
				1620	Older basin-fill deposits	Humboldt Formation
				3640	Volcanic rocks	Jarbidge Rhyolite
				3930	Older basin-fill deposits	Indian Well Formation
9	27-007-05214	5443	11926	0	Older basin-fill deposits	
				1800	Older basin-fill deposits	Hay Ranch Formation
				3100	Older basin-fill deposits	Humboldt Formation
				5202	Older basin-fill deposits	Indian Well Formation
				9070	Older basin-fill deposits	Elko Formation
10	27-007-05217	5557	10950	0	Younger basin-fill deposits	
				2102	Older basin-fill deposits	Humboldt Formation
				5041	Older basin-fill deposits	Indian Well Formation
				9053	Older basin-fill deposits	Elko Formation
				9430	Volcanic rocks	
				9538	Unspecified Paleozoic	
11	27-007-05223	5535	10320	0	Younger basin-fill deposits	
				3400	Older basin-fill deposits	Hay Ranch Formation
				6020	Older basin-fill deposits	Indian Well Formation
				8170	Unspecified Paleozoic	
12	27-007-05227	5482	10045	0	Unknown	

				1500	Volcanic rocks	
				4676	Older basin-fill deposits	Indian Well Formation
				8695	Older basin-fill deposits	Elko Formation
				8845	Upper Paleozoic carbonates	
13	27-007-05232	6034	12573	0	Younger basin-fill deposits	
				84	Volcanic rocks	
				172	Older basin-fill deposits	Elko Formation
				408	Mississippian clastic rocks	Diamond Peak Formation
				570	Mississippian clastic rocks	Chainman Sandstone
				3156	Mississippian clastic rocks	Chainman Shale
				3635	Lower Paleozoic carbonates	Tripon Pass Limestone
				5948	Lower Paleozoic carbonates	Guilmette Formation
				6968	Lower Paleozoic carbonates	Bay State Dolomite
				7372	Lower Paleozoic carbonates	Woodpecker Limestone
				7448	Lower Paleozoic carbonates	Sentinel Mountain Dolomite
				8128	Clastic sedimentary rocks	Oxyoke Canyon Formation
				8557	Lower Paleozoic carbonates	Beacon Peak Dolomite
				8923	Lower Paleozoic carbonates	Lone Mountain Dolomite
				10169	Lower Paleozoic carbonates	Roberts Mountain Formation
				11222	Lower Paleozoic carbonates	Ely Springs Dolomite
14	27-007-05234	5910	8865	0	Younger basin-fill deposits	
				115	Volcanic rocks	
				960	Older basin-fill deposits	Elko Formation
				1920	Mississippian clastic rocks	Diamond Peak Formation
				1972	Mississippian clastic rocks	Chainman Sandstone
				5255	Mississippian clastic rocks	Chainman Shale
				5940	Lower Paleozoic carbonates	Tripon Pass Limestone
				6759	Lower Paleozoic carbonates	Guilmette Formation
				8596	Clastic sedimentary rocks	Oxyoke Canyon Formation
				8682	Lower Paleozoic carbonates	Beacon Peak Dolomite
15	27-007-05244	6167	12281	0	Volcanic rocks	
				712	Mississippian clastic rocks	Diamond Peak Formation
				4018	Lower Paleozoic carbonates	Guilmette Formation
				7565	Mississippian clastic rocks	
16	27-007-05245	6619	8843	0	Mississippian clastic rocks	
				3600	Lower Paleozoic carbonates	
17	27-007-05248	6376	9050	0	Clastic sedimentary rocks	Woodruff Formation
				4518	Lower Paleozoic carbonates	Devil's Gate Limestone
				4905	Lower Paleozoic carbonates	Simonson Dolomite
				6086	Clastic sedimentary rocks	Oxyoke Canyon Formation
				6330	Lower Paleozoic carbonates	Beacon Peak Dolomite
				7492	Lower Paleozoic carbonates	Lone Mountain Dolomite
				8869	Lower Paleozoic carbonates	Hanson Creek Formation
18	27-007-05252	5955	4157	0	Younger basin-fill deposits	
				1710	Older basin-fill deposits	Elko Formation
				3700	Upper Paleozoic carbonates	Ely Limestone
19	27-007-05253	6174	10415	0	Volcanic rocks	
				1230	Mississippian clastic rocks	Chainman Formation
				8809	Lower Paleozoic carbonates	Tripon Pass Limestone
				10254	Lower Paleozoic carbonates	Devil's Gate Limestone

20	27-007-05261	5704	7492	0	Younger basin-fill deposits	
				5478	Volcanic rocks	
21	27-033-05278	5990	6250	0	Older basin-fill deposits	Hay Ranch Formation
				781	Older basin-fill deposits	Humboldt Formation
				1398	Upper Paleozoic carbonates	Ely Limestone
				2065	Mississippian clastic rocks	Diamond Peak Formation
				3373	Mississippian clastic rocks	Chainman Formation
				3426	Lower Paleozoic carbonates	Joana Limestone
				3682	Mississippian clastic rocks	Pilot Shale
				3861	Lower Paleozoic carbonates	Devil's Gate Limestone
				4653	Lower Paleozoic carbonates	Bay State Dolomite
				5437	Lower Paleozoic carbonates	Woodpecker Limestone
				5569	Lower Paleozoic carbonates	Sentinel Mountain Dolomite
22	27-033-05296	6103	2530	0	Younger basin-fill deposits	
				474	Older basin-fill deposits	Humboldt Formation
				964	Mississippian clastic rocks	Diamond Peak Formation
				2308	Mississippian clastic rocks	Chainman Formation
				2416	Lower Paleozoic carbonates	Joana Limestone
23	27-033-05320	6280	7090	0	Mississippian clastic rocks	Diamond Peak Formation
				1379	Mississippian clastic rocks	Chainman Formation
				2802	Mississippian clastic rocks	Webb Formation
				3244	Clastic sedimentary rocks	Woodruff Formation
				3494	Crystalline rocks	Eureka Quartzite
				3594	Lower Paleozoic carbonates	Devil's Gate Limestone
				5008	Lower Paleozoic carbonates	Bay State Dolomite
				5798	Lower Paleozoic carbonates	Woodpecker Limestone
				5882	Lower Paleozoic carbonates	Sentinel Mountain Dolomite
				6160	Clastic sedimentary rocks	Oxyoke Canyon Formation
				6260	Lower Paleozoic carbonates	Beacon Peak Dolomite
				6770	Lower Paleozoic carbonates	Lone Mountain Dolomite
24	27-007-05272	5352	11689	0	Unspecified basin-fill	
				6600	Older basin-fill deposits	Indian Well Formation
				7610	Older basin-fill deposits	Elko Formation
				8307	Upper Paleozoic carbonates	
				9750	Mississippian clastic rocks	Diamond Peak Formation
				10390	Mississippian clastic rocks	Chainman Formation
25	27-007-05274	5385	9100	0	Unspecified basin-fill	
				6860	Older basin-fill deposits	Indian Well Formation
				8510	Older basin-fill deposits	Elko Formation
				9060	Upper Paleozoic carbonates	

APPENDIX B

TOUGH2 Input Files for Methane Migration Models

```
2D Methane degassing base model - EWASG
ROCKS----1----*----2----*----3----*----4----*----5----*----6----*----7----*----8
HUMBO          2650.       .35  1.18E-12  1.18E-12  1.18E-12       2.0     1000.
INDWE          2650.       .20  1.18E-13  1.18E-13  1.18E-13       1.7     1000.
 ELKO          2650.       .20  5.90E-16  5.90E-16  5.90E-16       2.9     1000.
BOUND          2650.       .20    1.E-14    1.E-14    1.E-14       2.1     1.e55
FAULT          2650.       .20    5.E-12    5.E-12    5.E-12       2.1     1000.
FELKO          2650.       .20  5.90E-13  5.90E-13  5.90E-13       2.9     1000.

SELEC----1----*----2----*----3----*----4----*----5----*----6----*----7----*----8
    1                                          1    0    0    0    3    0    3
        .8   .8
MULTI----1----*----2----*----3----*----4----*----5----*----6----*----7----*----8
    3    4    3    6
START----1----*----2----*----3----*----4----*----5----*----6----*----7----*----8
----*----1 MOP: 123456789*123456789*1234 ---*----5----*----6----*----7----*----8
PARAM----1----*----2----*----3----*----4----*----5----*----6----*----7----*----8
 8 29999    99991000301000200 13 0  3  0                1.8
          2.20752e9        1.                          9.8         4
     1.E-5                          1.0               1.E-8
                1.e6                 0.               1.E-8                 45.
RPCAP----1----*----2----*----3----*----4----*----5----*----6----*----7----*----8
    7          0.627     0.045        1.      0.01
    7          0.627      0.04   1.48e-3      1.e7        1.
TIMES----1----*----2----*----3----*----4----*----5----*----6----*----7----*----8
    9
    8.64e4   6.048e5   2.592e6  1.5552e7  3.1536e7  3.1536e8  9.4608e8  1.5768e9
 2.20752e9

ENDCY
MESHM----1----*----2----*----3----*----4----*----5
XYZ
        0.
NX       1       10.
NY       1       10.
NZ       1     1.e-6
NZ     253       10.
NZ       1     1.e-6

#ENDFI----1----*----2----*----3----*----4----*----5----*----6----*----7----*----8
```

```
2D High K fault zone scenario - EWASG
ROCKS----1----*----2----*----3----*----4----*----5----*----6----*----7----*----8
HUMBO          2650.       .35  1.18E-12  1.18E-12  1.18E-12       2.0     1000.
INDWE          2650.       .20  1.18E-13  1.18E-13  1.18E-13       1.7     1000.
 ELKO          2650.       .20  5.90E-16  5.90E-16  5.90E-16       2.9     1000.
BOUND          2650.       .20    1.E-14    1.E-14    1.E-14       2.1     1.e55
FAULT          2650.       .20    1.E-11    1.E-11    1.E-11       2.1     1000.
FELKO          2650.       .20  5.90E-13  5.90E-13  5.90E-13       2.9     1000.

SELEC----1----*----2----*----3----*----4----*----5----*----6----*----7----*----8
    1                                             1    0    0    0    3    0    3
        .8   .8
MULTI----1----*----2----*----3----*----4----*----5----*----6----*----7----*----8
    3    4    3    6
START----1----*----2----*----3----*----4----*----5----*----6----*----7----*----8
----*----1 MOP: 123456789*123456789*1234 ---*----5----*----6----*----7----*----8
PARAM----1----*----2----*----3----*----4----*----5----*----6----*----7----*----8
 8 29999    99991000301000200 13 0  3  0                1.8
          2.04984e9       1.                           9.8         4
     1.E-5                          1.0               1.E-8
                1.e6                 0.               1.E-8                 45.
RPCAP----1----*----2----*----3----*----4----*----5----*----6----*----7----*----8
    7          0.627     0.045        1.      0.01
    7          0.627      0.04   1.48e-3      1.e7        1.
TIMES----1----*----2----*----3----*----4----*----5----*----6----*----7----*----8
    9
    8.64e4   6.048e5   2.592e6  1.5552e7  3.1536e7  3.1536e8  9.4608e8  1.5768e9
 2.20752e9

ENDCY
MESHM----1----*----2----*----3----*----4----*----5
XYZ
        0.
NX       1       10.
NY       1       10.
NZ       1     1.e-6
NZ     253       10.
NZ       1     1.e-6

#ENDFI----1----*----2----*----3----*----4----*----5----*----6----*----7----*----8
```

```
2D High K Indian Well Formation scenario - EWASG
ROCKS----1----*----2----*----3----*----4----*----5----*----6----*----7----*----8
HUMBO          2650.       .35  1.18E-12  1.18E-12  1.18E-12       2.0     1000.
INDWE          2650.       .20  2.36E-13  2.36E-13  2.36E-13       1.7     1000.
 ELKO          2650.       .20  5.90E-16  5.90E-16  5.90E-16       2.9     1000.
BOUND          2650.       .20    1.E-14    1.E-14    1.E-14       2.1     1.e55
FAULT          2650.       .20    5.E-12    5.E-12    5.E-12       2.1     1000.
FELKO          2650.       .20  5.90E-13  5.90E-13  5.90E-13       2.9     1000.

SELEC----1----*----2----*----3----*----4----*----5----*----6----*----7----*----8
    1                                             1    0    0    0    3    0    3
        .8   .8
MULTI----1----*----2----*----3----*----4----*----5----*----6----*----7----*----8
    3    4    3    6
START----1----*----2----*----3----*----4----*----5----*----6----*----7----*----8
----*----1 MOP: 123456789*123456789*1234 ---*----5----*----6----*----7----*----8
PARAM----1----*----2----*----3----*----4----*----5----*----6----*----7----*----8
 8 29999    99991000301000200 13 0  3  0                1.8
          2.20752e9        1.                          9.8         4
     1.E-5                          1.0               1.E-8
                 1.e6                0.               1.E-8                 45.
RPCAP----1----*----2----*----3----*----4----*----5----*----6----*----7----*----8
    7          0.627     0.045        1.      0.01
    7          0.627      0.04   1.48e-3      1.e7        1.
TIMES----1----*----2----*----3----*----4----*----5----*----6----*----7----*----8
    9
    8.64e4   6.048e5   2.592e6  1.5552e7  3.1536e7  3.1536e8  9.4608e8  1.5768e9
 2.20752e9

ENDCY
MESHM----1----*----2----*----3----*----4----*----5
XYZ
        0.
NX       1       10.
NY       1       10.
NZ       1     1.e-6
NZ     253       10.
NZ       1     1.e-6

#ENDFI----1----*----2----*----3----*----4----*----5----*----6----*----7----*----8
```

```
2D No Fault Methane Degassing - EWASG
ROCKS----1----*----2----*----3----*----4----*----5----*----6----*----7----*----8
HUMBO          2650.       .35  1.18E-12  1.18E-12  1.18E-12       2.0     1000.
INDWE          2650.       .20  1.18E-13  1.18E-13  1.18E-13       1.7     1000.
 ELKO          2650.       .20  5.90E-16  5.90E-16  5.90E-16       2.9     1000.
BOUND          2650.       .20    1.E-14    1.E-14    1.E-14       2.1     1.e55
FELKO          2650.       .20  5.90E-13  5.90E-13  5.90E-13       2.9     1000.

SELEC----1----*----2----*----3----*----4----*----5----*----6----*----7----*----8
    1                                          1    0    0    0    3    0    3
        .8   .8
MULTI----1----*----2----*----3----*----4----*----5----*----6----*----7----*----8
    3    4    3    6
START----1----*----2----*----3----*----4----*----5----*----6----*----7----*----8
----*----1 MOP: 123456789*123456789*1234 ---*----5----*----6----*----7----*----8
PARAM----1----*----2----*----3----*----4----*----5----*----6----*----7----*----8
 8 29999    99991000301000200 13 0  3  0                1.8
          2.20752e9       1.                           9.8         4
     1.E-5                          1.0               1.E-8
                1.e6                 0.               1.E-8                 45.
RPCAP----1----*----2----*----3----*----4----*----5----*----6----*----7----*----8
    7          0.627     0.045        1.      0.01
    7          0.627      0.04   1.48e-3      1.e7        1.
TIMES----1----*----2----*----3----*----4----*----5----*----6----*----7----*----8
    9
    8.64e4   6.048e5   2.592e6  1.5552e7  3.1536e7  3.1536e8  9.4608e8  1.5768e9
 2.20752e9

ENDCY
MESHM----1----*----2----*----3----*----4----*----5
XYZ
        0.
NX       1       10.
NY       1       10.
NZ       1     1.e-6
NZ     253       10.
NZ       1     1.e-6

#ENDFI----1----*----2----*----3----*----4----*----5----*----6----*----7----*----8
```

APPENDIX C

Spatial Distributions of Methane Gas Saturation in TOUGH2 Simulations

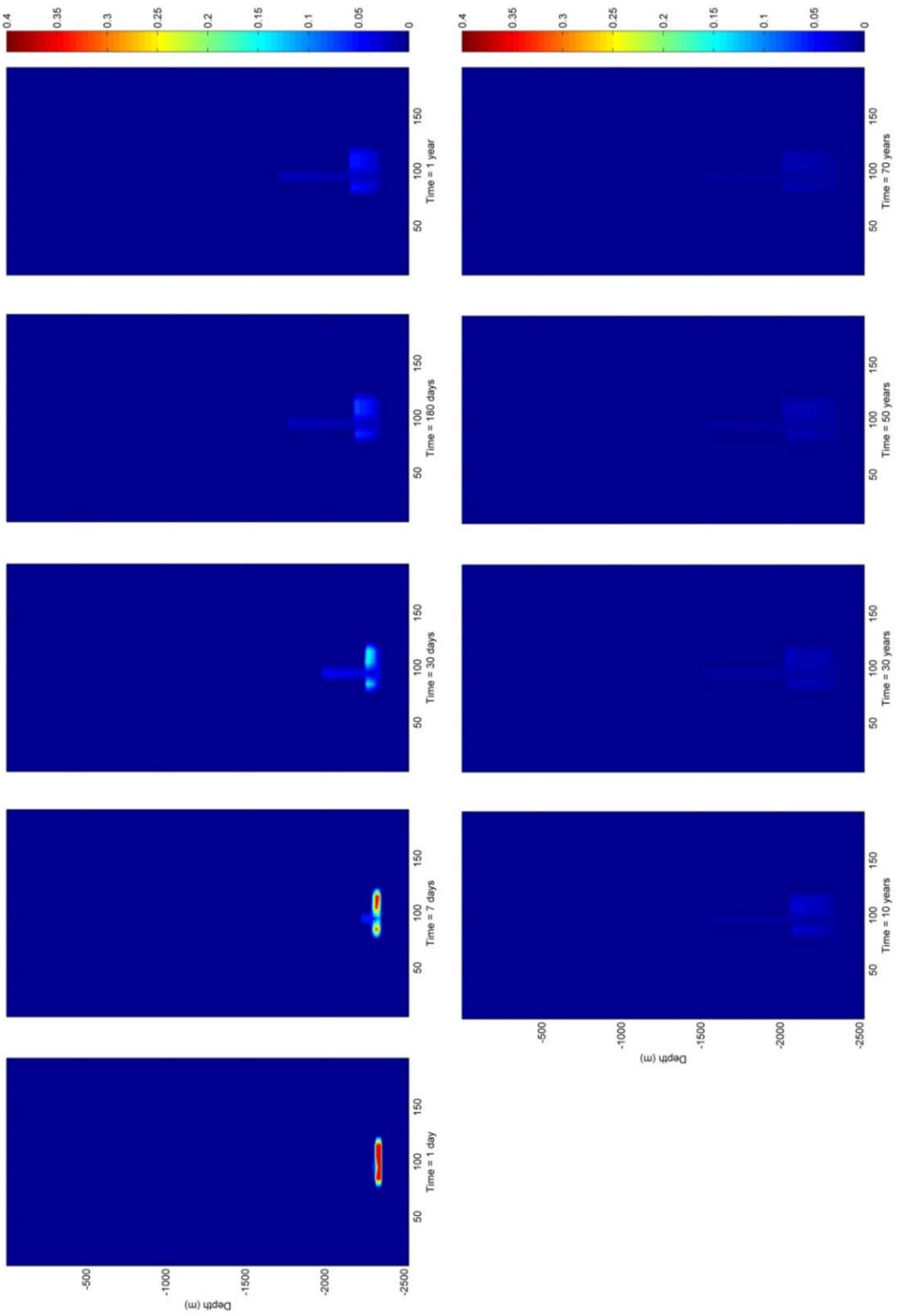

Figure 24. Methane gas saturation for Base Scenario, Sg = 0.4

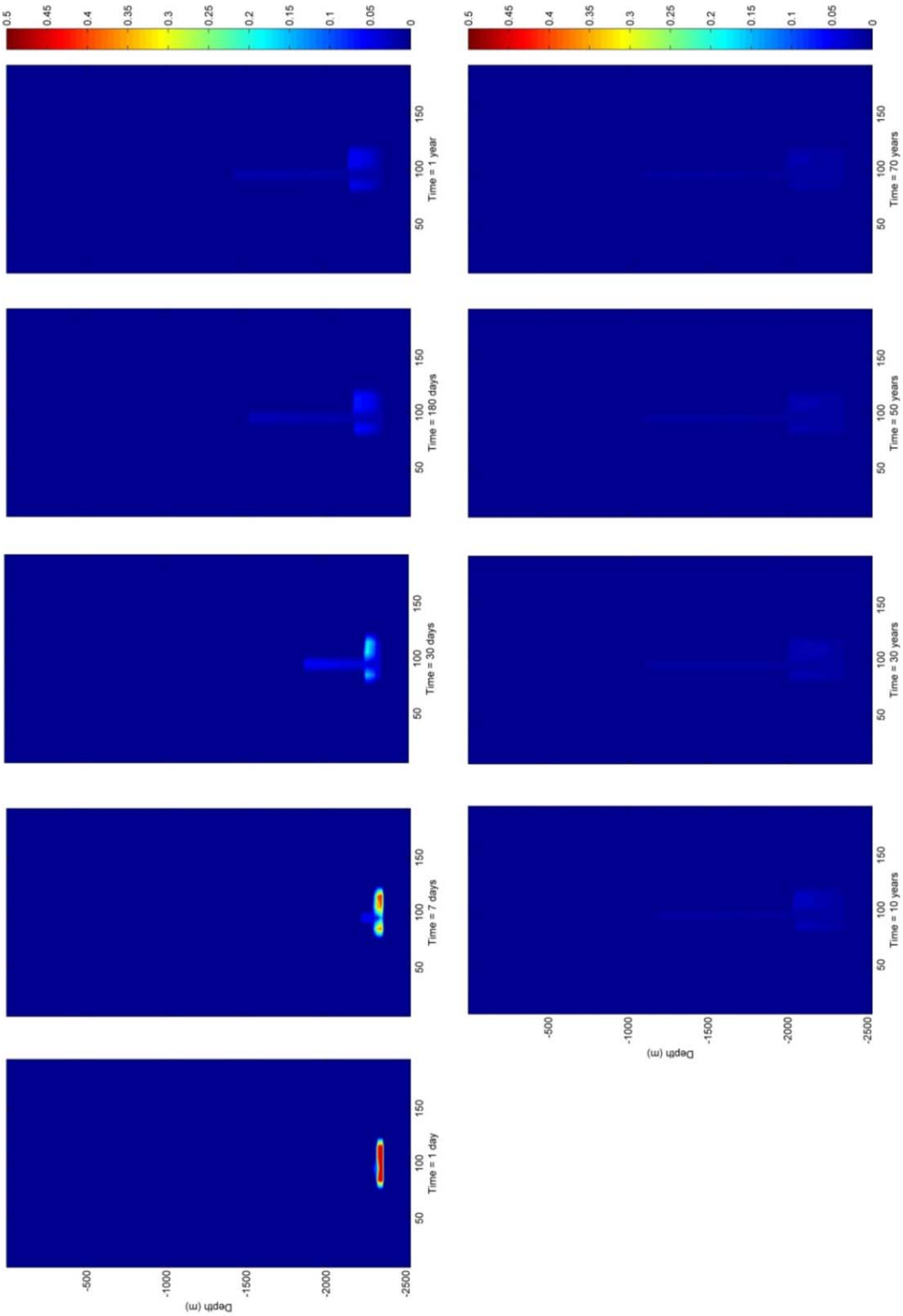

Figure 25. Methane gas saturation for Base Scenario, Sg = 0.5

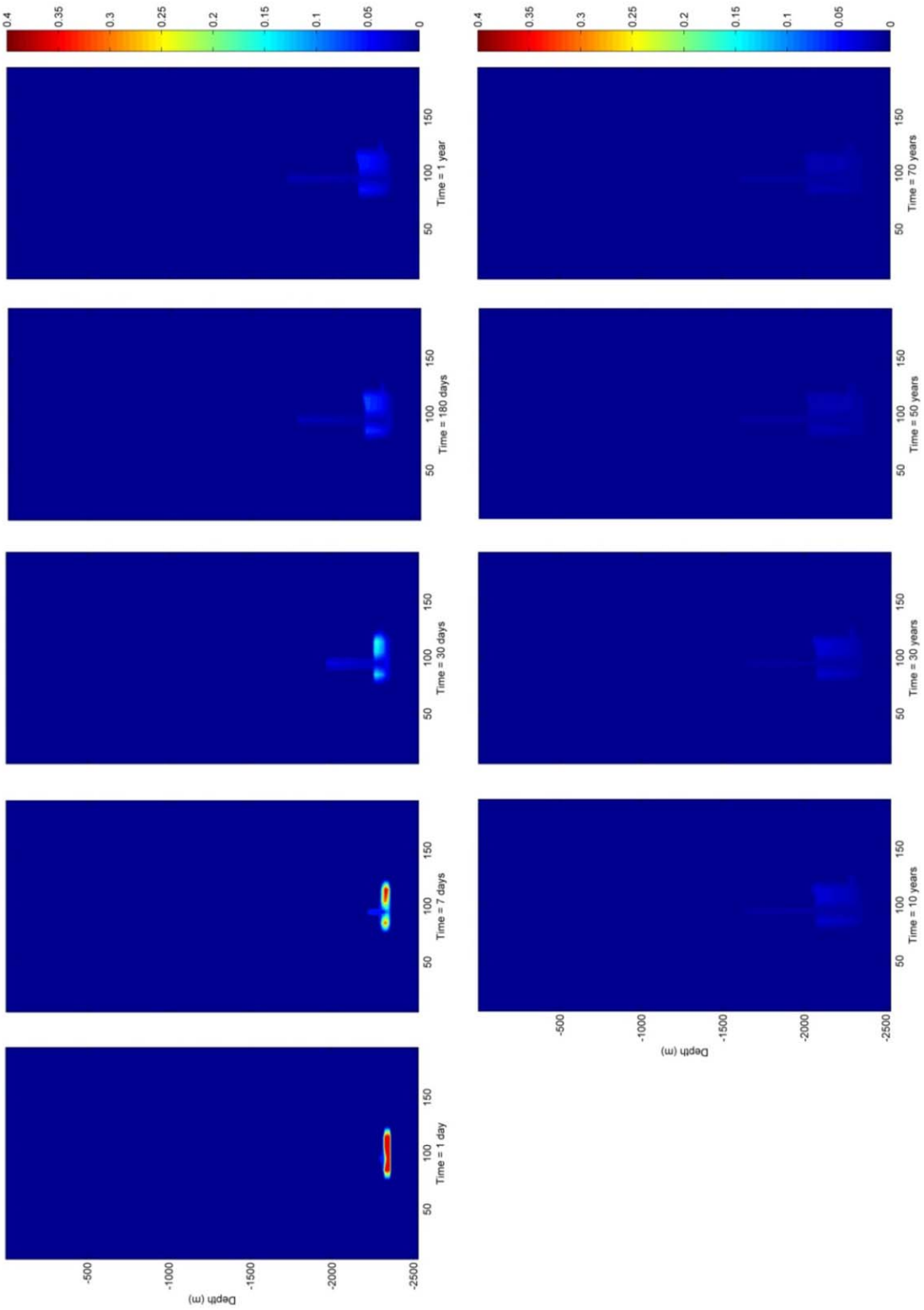

Figure 26. Methane gas saturation for High Conductivity Fault Scenario, Sg = 0.4

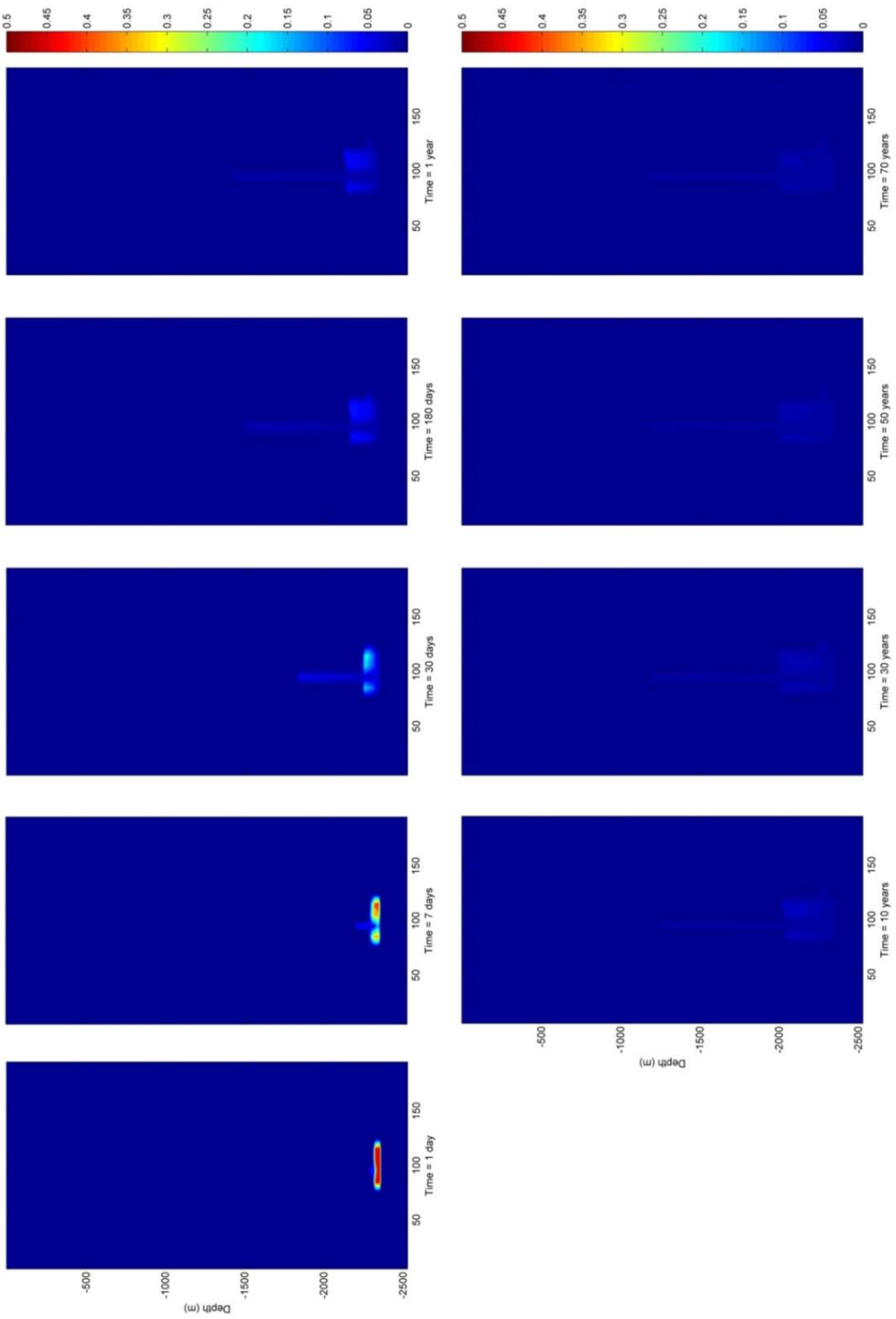

Figure 27. Methane gas saturation for High Conductivity Fault Scenario, Sg = 0.5

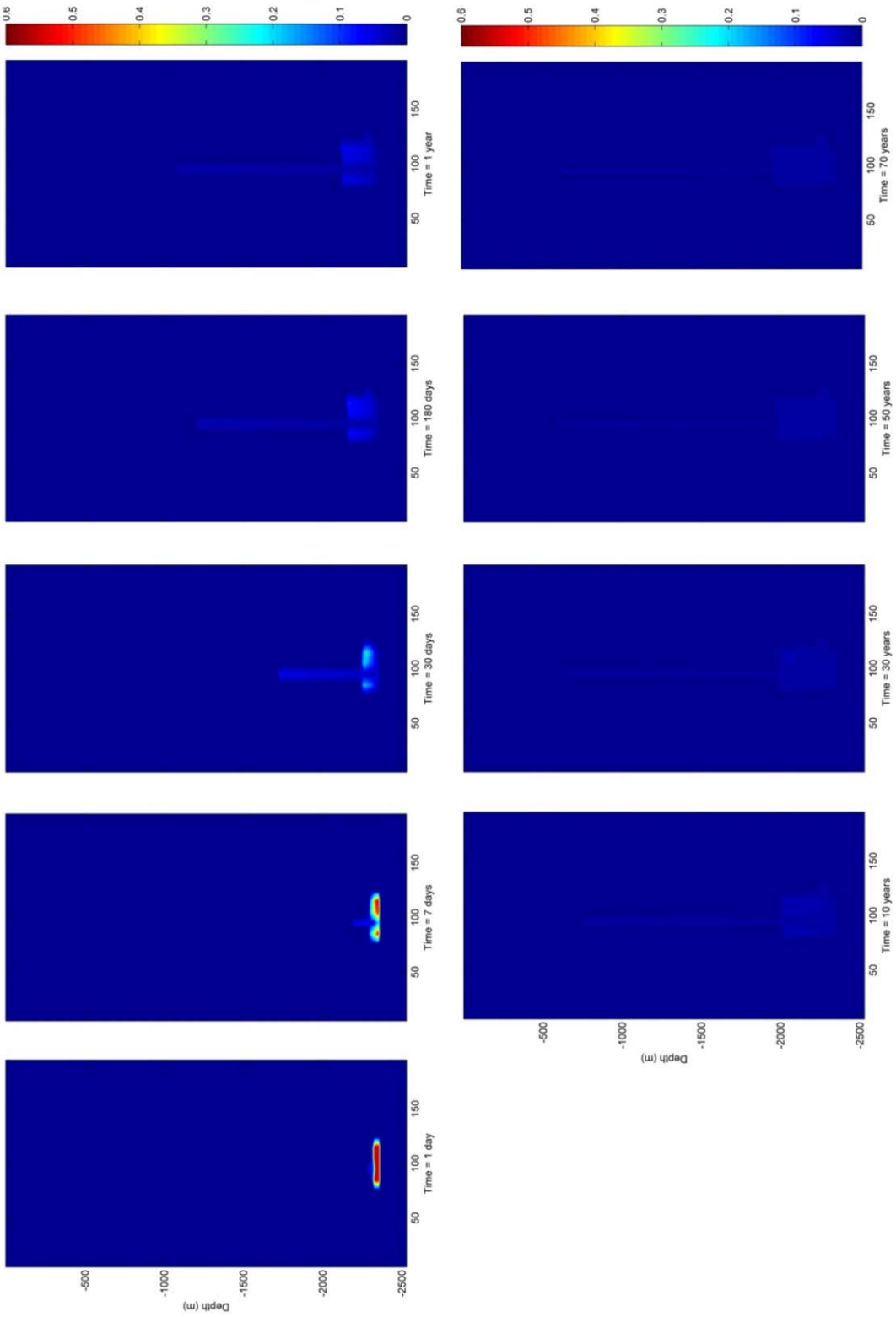

Figure 28. Methane gas saturation for High Conductivity Fault Scenario, Sg = 0.6

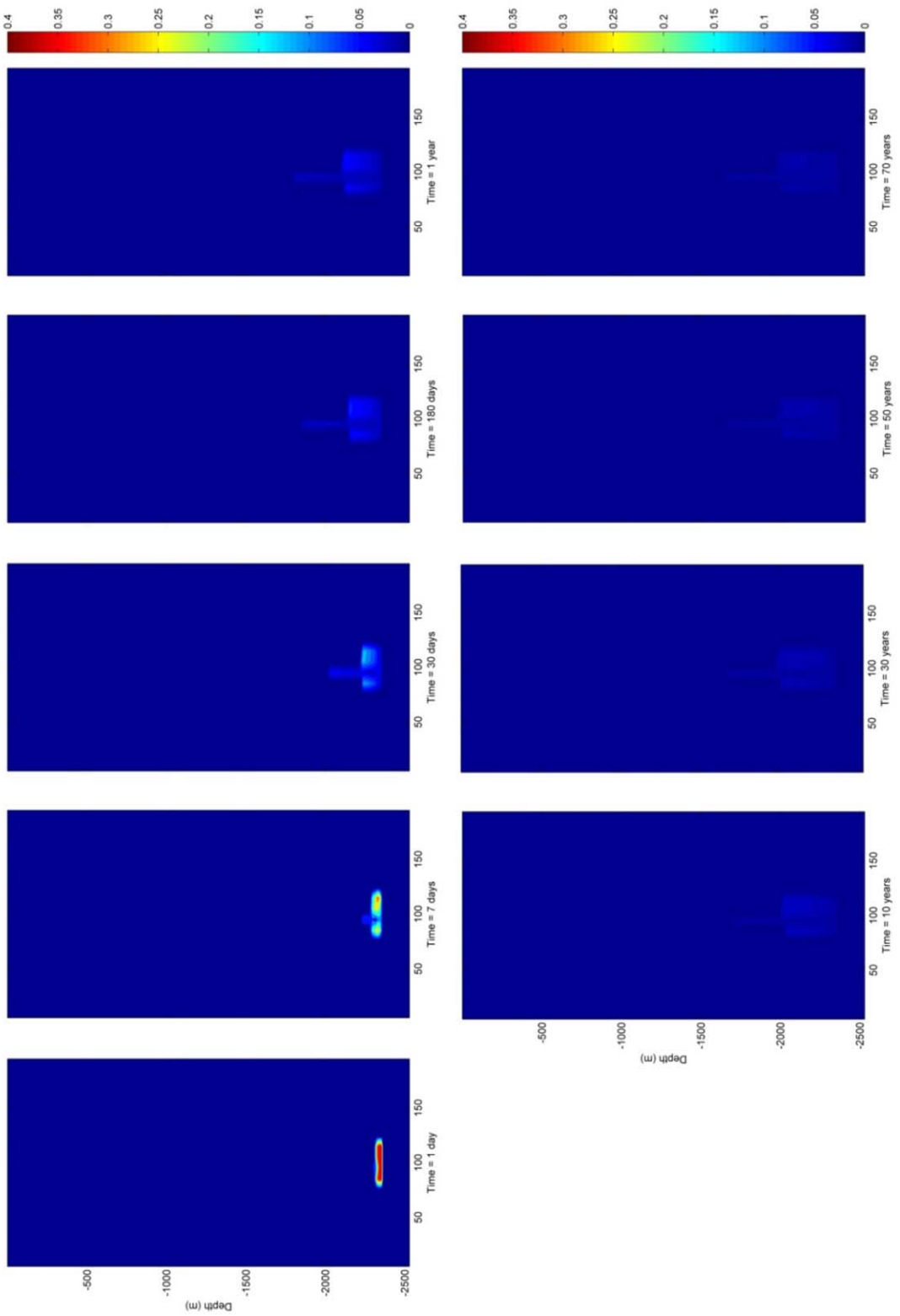

Figure 29. Methane gas saturation for High Conductivity Indian Well Scenario, Sg = 0.4

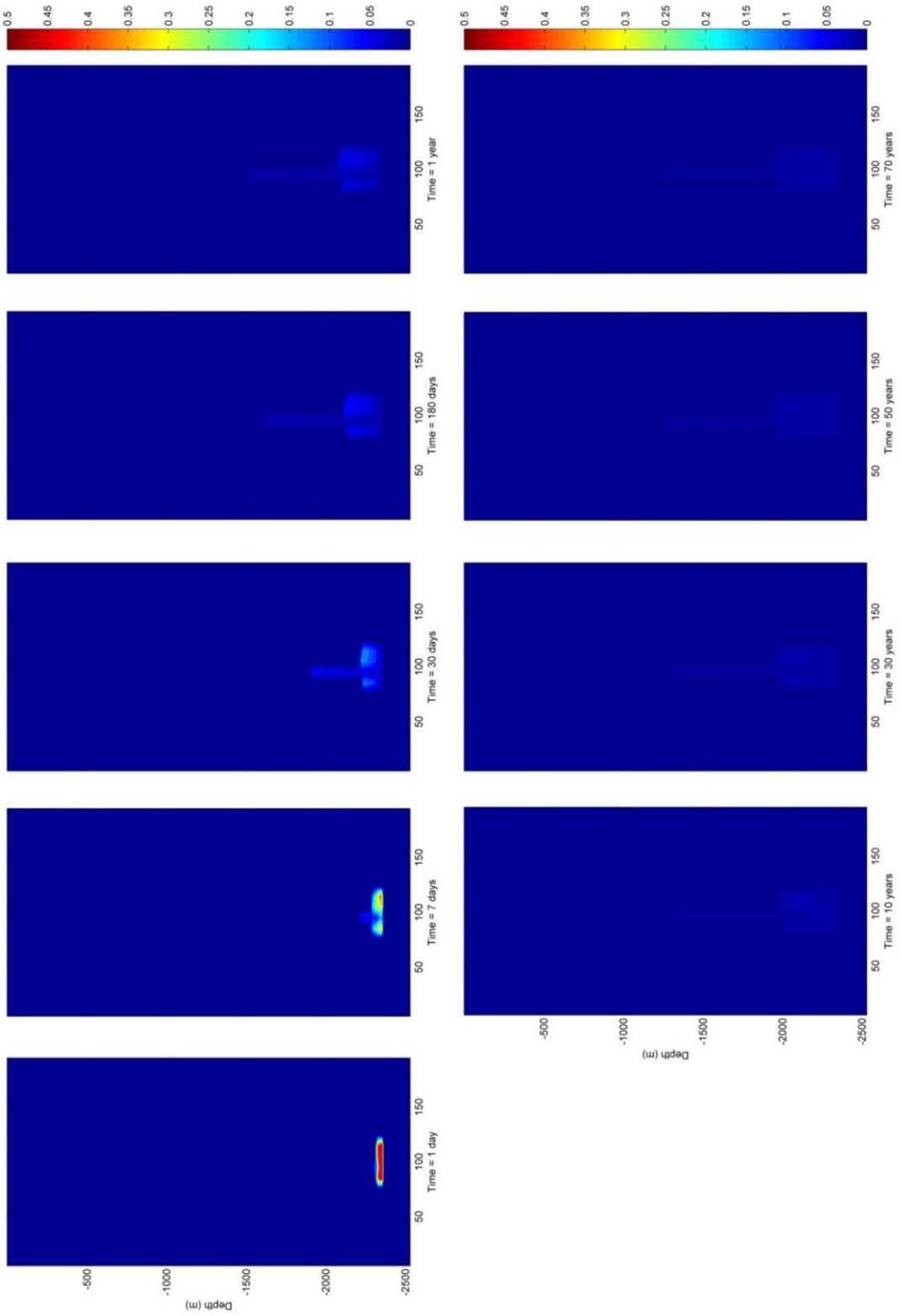

Figure 30. Methane gas saturation for High Conductivity Indian Well Scenario, Sg = 0.5

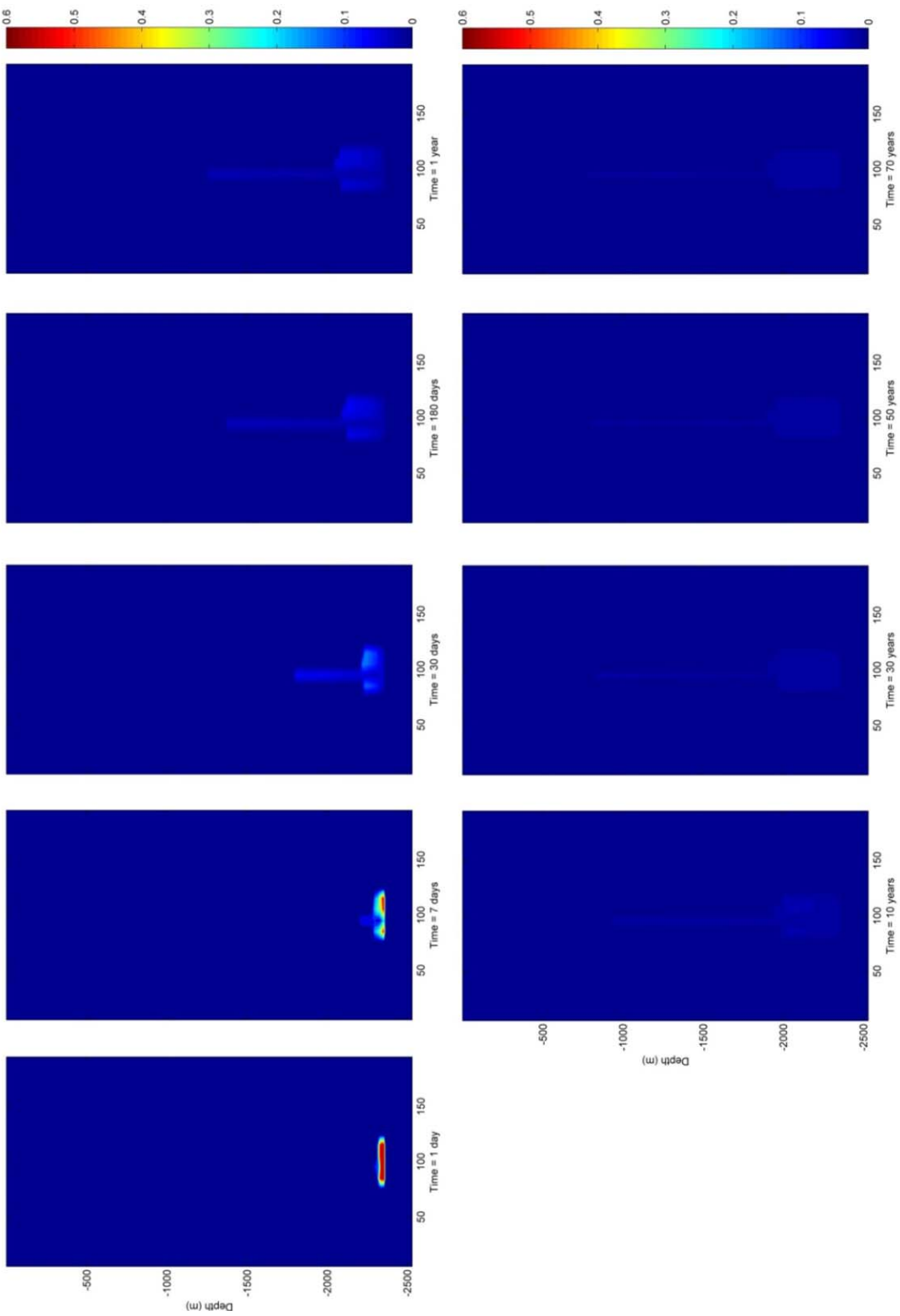

Figure 31. Methane gas saturation for High Conductivity Indian Well Scenario, Sg = 0.6